The Great Slump: Mrk 926 reveals discrete and varying Balmer line satellite components during a drastic phase of decline[*,**]

Wolfram Kollatschny[1], Martin W. Ochmann[1,2], Shai Kaspi[3], Claas Schumacher[1], Ehud Behar[4], Doron Chelouche[5], Keith Horne[6], Björn Müller[1,7], Stephen E. Rafter[4], Rolf Chini[2,8], Martin Haas[2], and Malte A. Probst[1]

[1] Institut für Astrophysik, Universität Göttingen, Friedrich-Hund Platz 1, 37077 Göttingen, Germany
e-mail: wkollat@astro.physik.uni-goettingen.de
[2] Astronomisches Institut, Ruhr-Universität Bochum, Universitätsstrasse 150, 44801 Bochum, Germany
[3] School of Physics & Astronomy and the Wise Observatory, The Raymond and Beverly Sackler Faculty of Exact Sciences Tel-Aviv University, Tel-Aviv 69978, Israel
[4] Technion, Institute of Technology, Haifa 3200003, Israel
[5] Physics Department and the Haifa Research Center for Theoretical Physics and Astrophysics, University of Haifa, Haifa 3498838, Israel
[6] SUPA School of Physics and Astronomy, University of St. Andrews, St. Andrews, Fife KY16 9SS, UK
[7] Max-Planck-Institut für Sonnensystemforschung, Justus-von-Liebig-Weg 3, 37077 Göttingen, Germany
[8] Instituto de Astronomía, Universidad Católica del Norte, Avenida Angamos 0610, Antofagasta, Chile

ABSTRACT

Aims. Mrk 926 is known to be a highly variable active galactic nucleus. Furthermore, it is known to show very broad line profiles. We intended to study the continuum and line profile variations of this object with high temporal resolution in order to determine its broad-line region structure and to derive its black hole mass.
Methods. We carried out a high-cadence spectroscopic variability campaign of Mrk 926 with the 10m HET telescope, aided by photometric *V*-band data taken with the C18 telescope at the Wise Observatory, over a period of about five months. We extracted spectroscopic continuum and line light curves, and computed cross-correlation functions (CCFs) as well as velocity-resolved CCFs with respect to the combined spectroscopic and photometric *V*-band light curve.
Results. The continuum luminosity of Mrk 926 showed a drastic decrease during our campaign. The luminosity dropped to less than 50% of its original luminosity within only 2.5 months. Furthermore, the spectra of Mrk 926 show complex and very broad Balmer line profiles, including outer Balmer satellites ranging from ±5000 to ±13 000 km s^{-1}. The integrated Hα, Hβ, and He I λ5876 line light curves are delayed relative to the continuum light curve. The Hα and Hβ lines show two velocity-delay structures in the central part of their line profile (within ±5000 km s^{-1}), at ∼10 and ∼57 light-days and at ∼5 and ∼48 light-days, respectively. These structures might be interpreted as the upper and lower halves of an ellipse in the velocity-delay plane, which might be the signature of a line-emitting ring, inclined by ∼50° to the line of sight and orbiting the black hole at radii, *R*, of 33.5 and 26.5 light-days. We determined continuum luminosities, log(λL_λ/erg s^{-1}), of 43.68–44.13, which are in good agreement with the established $R_{\rm BLR} - L_{\rm AGN}$ relation. Adopting delays of 33.5 and 26.5 days for Hα and Hβ, respectively, we derive a black hole mass of $(1.1 \pm 0.2) \times 10^8 \, M_\odot$; this indicates a low Eddington ratio, which decreased from 8 to 3 percent during our campaign. The Balmer satellite components show a higher correlation coefficient with respect to the continuum than the central line profile, and their response to the continuum variations is on the order of only 3−5 days. We attribute this to the central line segment and the Balmer satellites having different, spatially distinct regions of origin.

Key words. galaxies: active – galaxies: Seyfert – galaxies: nuclei – galaxies: individual: Mrk926 – quasars: emission lines

1. Introduction

Active galactic nuclei (AGN) are variable in all frequency bands on timescales of days to years. It is generally accepted that the variability of the central ionizing continuum source causes line intensity variations in the broad emission lines. Furthermore, changes in the kinematics and structure in the broad-line region (BLR) as well as obscuration can induce variations in the line profiles. However, many details of the innermost BLR, such as size, structure, and kinematics, are poorly understood. In addition, most of the variability campaigns carried out in the past were devoted to Seyfert galaxies that show broad emission lines with full widths at half maximum (FWHMs) of 1000–4000 km s^{-1}, and only very few reverberation campaigns have been carried out for AGN with very broad lines ($FWHM \gg 4000$ km s^{-1}; e.g., 3C390.3: Sergeev et al. 2002; Gezari et al. 2007, and other AGN therein). Broad-line reverberation studies exist for more than 50 Seyfert galaxies (e.g., Peterson et al. 2002; Kaspi et al. 2005; Denney et al. 2009; Barth et al. 2011; Bentz et al. 2013; Shapovalova et al. 2013; Shen et al. 2016; Du et al. 2018, and references therein). However, detailed velocity-resolved reverberation mapping studies have been carried out for only

---

[*] The reduced spectra and the photometric light curve are only available at the CDS via anonymous ftp to cdsarc.u-strasbg.fr (130.79.128.5) or via http://cdsarc.u-strasbg.fr/viz-bin/cat/J/A+A/657/A122

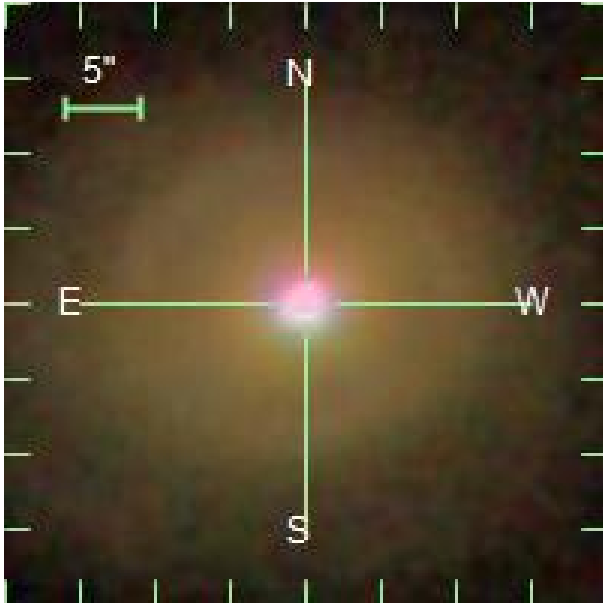[**] Based on observations obtained with the *Hobby-Eberly* Telescope.

Fig. 1. Composite SDSS image of Mrk 926 taken from the SDSS SkyServer[2]. The crosshairs are centered on the nucleus.

about a dozen Seyfert galaxies (e.g., Mrk 110: Kollatschny 2003; Arp 151: Bentz et al. 2008; Mrk 335, Mrk 1501, 3C 120, PG 2130: Grier et al. 2013b; 3C120: Kollatschny et al. 2014; Mrk 335, Mrk 1044, Mrk 142: Xiao et al. 2018; HE1136-2304: Kollatschny et al. 2018; NGC 5548: Horne et al. 2021 and references therein).

Mrk 926 can be classified as either a strong Seyfert 1 galaxy or a quasar based on its luminosity during the campaign presented here (see Sect. 4.4). Its Balmer and He I lines have widths (FWHM) of more than $5000 \, km \, s^{-1}$. In a study on the long-term variability of very broad-line AGN (Kollatschny et al. 2006), Mrk 926 additionally exhibited strong Hβ line variability amplitudes. The nuclear activity in Mrk 926 was detected by Ward et al. (1978) when they took a spectrum of the optical counterpart of a strong X-ray source. Mrk 926 is a compact source on direct images in the optical (Garnier et al. 1996). We show an SDSS (DR16: Ahumada et al. 2020) image of Mrk 926 in Fig. 1. Based on SDSS r-band images, it has an isophotal diameter (major axis) of 57.12 arcsec. This corresponds to 53 kpc. The deVaucouleurs diameter amounts to 6.00 arcsec, corresponding to 5.56 kpc[1]. Mrk 926 is the brighter galaxy member (RA = 23:04:43.5, Dec = −08:41:09 (2000), z = 0.04701) in a double system with PGC 1000273. This close starburst companion is located one arcmin to the south.

Osterbrock & Shuder (1982) published the first emission-line profiles of Mrk 926. They reported that the lines did not vary between July 1978 and December 1979. We were able to show that Mrk 926 varied by a factor of 2 in the continuum as well as by a factor of 2.5 in the Balmer lines over a period of eight years between 1990 and 1997 (Kollatschny et al. 2006). In a follow-up paper (Kollatschny & Zetzl 2010), we focused on line profile variations in Mrk 926 as the line profiles of AGN and their variations can give us information about the structure of the line-emitting region. We intensively studied the variations in individual line segments of the Balmer lines and the changes in

the profiles during a variability campaign in 2005 and another shorter campaign conducted in 2004.

Here, we selected Mrk 926 (MCG-2-58-22) as a target for an even more detailed, combined spectroscopic and photometric variability study of an AGN that shows very broad emission lines. The paper is structured as follows: In Sect. 2 we describe the observations and data reduction. The results of the variability and reverberation mapping study are presented in Sect. 3. We discuss the results in Sect. 4 and give a summary in Sect. 5. Throughout this paper, we assume a Λ cold dark matter cosmology with a Hubble constant of $H_0 = 73 \, km \, s^{-1} \, Mpc^{-1}$, $\Omega_\Lambda = 0.73$, and $\Omega_M = 0.27$. With a redshift of $z = 0.04701$, this results in a luminosity distance of $D_L = 200.2 \, Mpc = 6.18 \times 10^{26} \, cm$ using the cosmology calculator developed by Wright (2006).

2. Observations and data reduction

2.1. Spectroscopic observations with HET

We took optical spectra of Mrk 926 with the 9.2 m *Hobby-Eberly* Telescope (HET) located at the McDonald Observatory at 31 epochs between 2010 July 19 and November 19. Thus, we obtained 31 spectra over a period of 122.7 days. The date of the campaign was fixed by the allocated observing time slots. The average interval between the observations was 4.1 days. Excluding the first two observations, the average time interval between observations reduces to 2.7 days with a majority of consecutive observations only 1-2 days apart. The log of our spectroscopic observations is given in Table 1. All spectroscopic observations were taken with identical instrumental setups. We used the Marcario Low Resolution Spectrograph (LRS) attached at the prime focus of HET. The detector was a 3072×1024 15 μm pixel Ford Aerospace charge-coupled device (CCD) with 2×2 binning. The spectra cover the wavelength range from 4160 Å to 6930 Å (LRS grism 2 configuration) in the rest frame of the galaxy (and 4350 Å–7250 Å observed frame) with a resolving power of 650 at 5000 Å (7.7 Å FWHM). Nearly all observations were taken with an exposure time of 20 min, which in most cases yielded a S/N of >100 per resolution element in the continuum. The slit width was fixed to 2″0 projected on the sky at an optimized position angle to minimize differential refraction. Furthermore, all observations were taken at the same airmass owing to the particular design of the HET. Typical seeing values ranged from 1″4 to 1″9.

In addition to the spectra of Mrk 926, necessary calibration images including bias, flat, and arc frames (CdHgAr and Xe), as well as spectrophotometric standard stars (Hiltner 600) for flux calibration were taken. We reduced the spectra (bias subtraction, cosmic ray correction, flat-field correction, 2D-wavelength calibration, night sky subtraction, flux calibration, etc.) in a homogeneous way with standard IRAF[3] reduction packages (Tody 1986, 1993) like we did in previous publications (e.g., Kollatschny et al. 2001). In addition, we corrected for atmospheric absorption in the oxygen *B* band by fitting the continuum of the standard star Hiltner 600 and using this fit to normalize its spectrum. In this way, we created a template of the oxygen absorption that we scaled to each object spectrum individually. The spatial resolution per binned pixel was 0″472. We extracted four columns in our object spectra. This conforms to the slit width. Great care was taken to ensure high-quality intensity and wavelength calibrations to keep the intrinsic measurement errors

---

Table 1. Log of spectroscopic HET observations of Mrk 926.

Mod. Julian date	UT date	Exp. time [sec.]
55396.41	2010-07-19	1200
55397.42	2010-07-20	1200
55441.31	2010-09-02	1200
55443.30	2010-09-04	1200
55444.30	2010-09-05	1200
55445.28	2010-09-06	1200
55446.29	2010-09-07	1200
55451.27	2010-09-12	1200
55452.26	2010-09-13	1200
55453.26	2010-09-14	1200
55467.23	2010-09-28	1800
55470.20	2010-10-01	1200
55471.21	2010-10-02	1200
55472.22	2010-10-03	1200
55477.20	2010-10-08	1200
55480.20	2010-10-11	1800
55481.20	2010-10-12	951
55483.20	2010-10-14	1300
55494.16	2010-10-25	1200
55496.15	2010-10-27	1200
55497.16	2010-10-28	1200
55498.17	2010-10-29	1200
55499.16	2010-10-30	1200
55501.14	2010-11-01	1200
55505.12	2010-11-05	1200
55506.12	2010-11-06	1200
55507.11	2010-11-07	1200
55508.11	2010-11-08	1200
55514.12	2010-11-14	1200
55515.10	2010-11-15	1200
55519.10	2010-11-19	1200

very low (e.g., Kollatschny et al. 2001; Kollatschny & Zetzl 2010). The spectra were not always taken under photometric conditions. Therefore, we calibrated all spectra to the same absolute forbidden narrow-line fluxes under the assumption of a non-varying narrow-line flux on timescales of years. We chose [O III] $\lambda4959$ and [O III] $\lambda5007$, as well as [O I] $\lambda6300/63$, [N II] $\lambda6548/84$, and [S II] $\lambda6717/31$ as calibration lines for the blue and red section of the spectrum, respectively. The blue part of the spectrum was scaled to an [O III] $\lambda5007$ flux of 3.14×10^{-13} erg s^{-1} cm^{-2}. The same flux value has been used before for Mrk 926 in Kollatschny et al. (2006) and Kollatschny & Zetzl (2010). Durret & Bergeron (1988) and Morris & Ward (1988) derived similar [O III] $\lambda5007$ fluxes from their Mrk 926 spectra: 2.05×10^{-13} erg s^{-1} cm^{-2} and 3.31×10^{-13} erg s^{-1} cm^{-2}, respectively. We note that hereafter all continuum flux densities and line fluxes at wavelengths >6500 Å (observed frame) refer to the intercalibration with respect to [O I] $\lambda6300/63$, [N II] $\lambda6548/84$, and [S II] $\lambda6717/31$. The accuracy of the flux calibration was tested for all forbidden emission lines in the spectra. We calculated difference spectra for all epochs with respect to the mean spectrum of our variability campaign. Corrections for small spectral shifts (<0.5 Å) and small scaling factors were implemented by minimizing the residuals of the narrow emission lines in the difference spectra. A relative flux accuracy of 1–2% was obtained for most of our spectra.

2.2. Photometric observations at the Wise Observatory

Mrk 926 was observed with a Bessell *V*-band filter (Bessell 1990) at the C18 telescope (Brosch et al. 2008) of the Wise Observatory in Israel, from 2010 August 28 to December 10. Observations were carried out daily with gaps due to bad weather on some nights. The SBIG STL-6303 CCD was used with 3072×2048 9 µm pixel, and plate-scale of 1.47 arcsec pix^{-1}, which gives a field of view of 75×50 arcmin. Each night several exposures of 5 min each were obtained. The *V*-band filter has a bandwidth ranging from 4700 Å to 6500 Å and an effective central wavelength of 5415 Å. The contribution of the total Hβ flux to the *V* band can be estimated to be <10%. Since the variable part of Hβ only accounts for 30–40 % of the total Hβ flux during our campaign (see Table 5) the variable Hβ contribution to the *V* band is <4% and is therefore negligible.

Data reduction was carried out in the standard way for bias, dark, and flat-field, using standard IRAF routines. In order to measure the instrumental magnitude of the objects in each image we used the DAOPHOT package (Stetson 1987) as implemented in IRAF. We derived the point-spread function for each image and measured all available objects in the image. We then used the DAOSTAT program (Netzer et al. 1996) to choose the non-variable stars in the field and use them to inter-calibrate by differential photometry the instrumental magnitude of Mrk 926 between the images and to get its light curve. Measurements from the same night were averaged to obtain a single measurement for each night in order to decrease the uncertainty on each point in the light curve.

3. Results

3.1. Continuum and spectral line variations

We present all the reduced [O III] $\lambda5007$-intercalibrated optical spectra of our variability campaign from Mrk 926 in Fig. 2. They clearly show variations in the continuum intensities. The mean and rms spectra of Mrk 926 are shown in Fig. 3[4]. The rms spectrum indicates the variable part of the emission lines. It was scaled to allow for a better comparison with the mean spectrum and to enhance weaker line structures. The continuum regions and integration limits of the broad emission lines used in our present study are given in Table 2 and shown at the bottom of the spectra in Fig. 2. We selected the continuum regions by inspecting the mean and rms spectra for regions that are free of both strong emission and absorption lines.

A continuum region at 5100 Å (rest frame) is often used in studies of the variable continuum flux in AGN. Normally, this region is free of strong emission lines and close to the [O III] $\lambda5007$ flux calibration line. However, in our case this region is contaminated by Hβ because of the very broad line profile widths in Mrk 926. Thus, we settled for a continuum range slightly more shifted to the red part of the spectrum (5180 Å in the rest frame). Finally, we determined the continuum intensities at seven wavelength ranges (at 4425, 4755, 5420, 5485, 5755, 6530 and 7255 Å in the observed frame). We integrated the broad emission-line intensities of the Balmer and He I lines

---

[4] The presented mean and rms spectra are a combination of the blue and red intercalibrations. We merged them at 6345 Å and used a small scaling factor to adapt the redward calibration to the intercalibration with respect to [O III] $\lambda5007$.
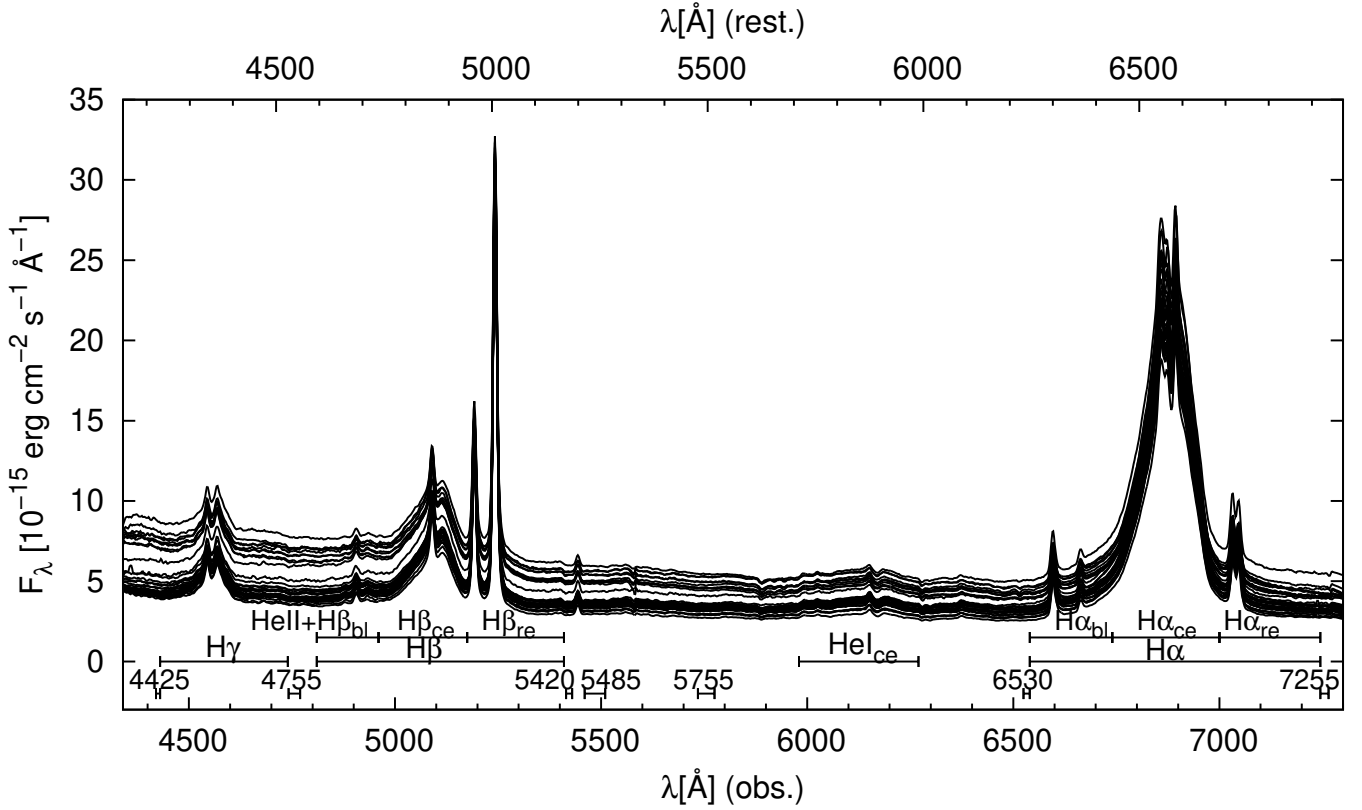
Fig. 2. Reduced and [O III] $\lambda5007$-intercalibrated optical spectra of Mrk 926 taken with the HET telescope during our variability campaign in 2010. The continuum bands and the broad-line integration intervals are marked according to Table 2. The spectra shown here are not corrected for Galactic foreground extinction.
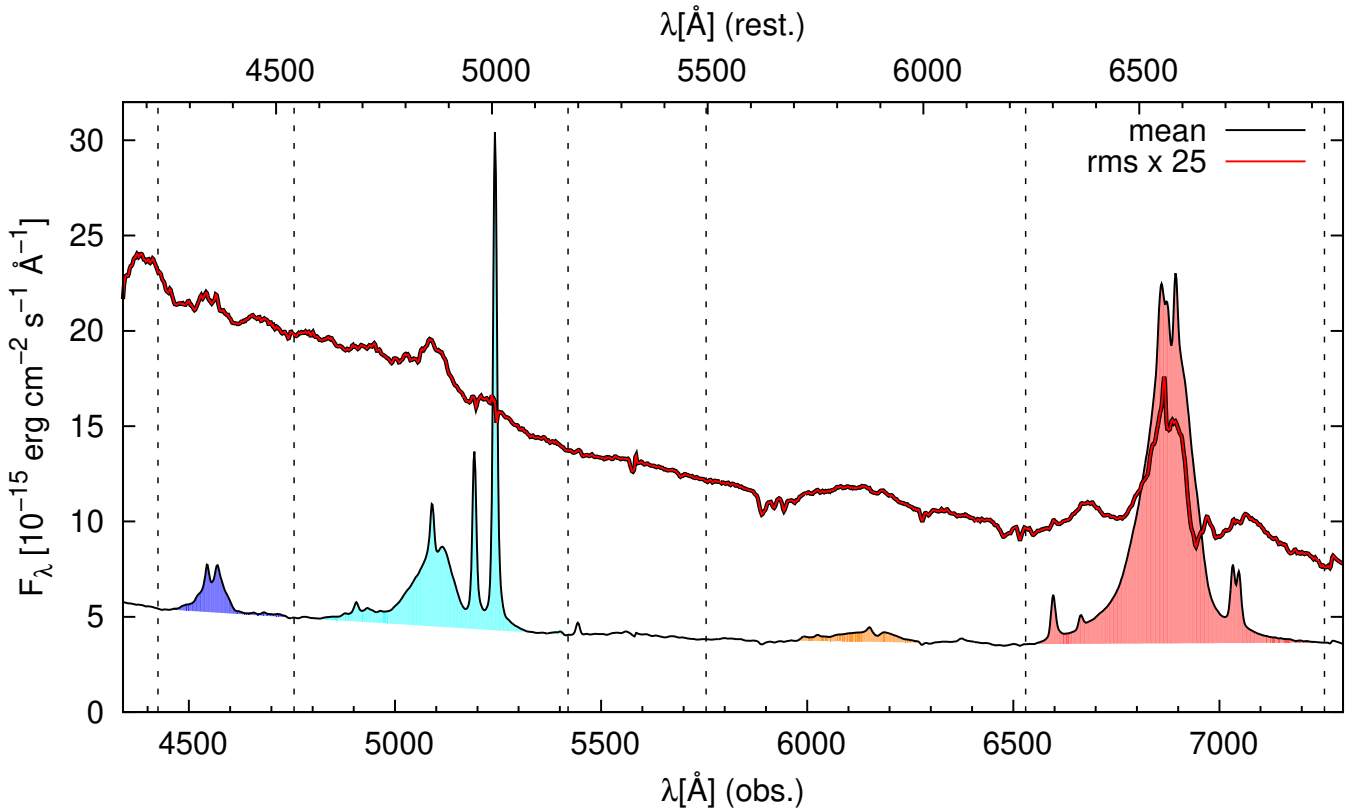

Fig. 3. Combined mean spectrum (black) and rms spectrum (red; see Sect. 3.1 for details) of Mrk 926 from our variability campaign. The rms spectrum was scaled to allow for a direct comparison. The central wavelengths of the pseudo-continua used for linear continuum subtraction are denoted by the vertical dashed lines. The line integration limits are marked by the shaded areas.

Table 2. Continuum boundaries, line integration limits, and pseudo-continua.

Cont./Line (1)	Wavelength range (2)	Pseudo-continuum (3)
Cont. 4425 (4225)	4420–4430	
Cont. 4755 (4540)	4742–4770	
Cont. 5420 (5180)	5415–5430	
Cont. 5485 (5240)	5460–5510	
Cont. 5755 (5500)	5735–5775	
Cont. 6530 (6240)	6525–6540	
Cont. 7255 (6930)	7245–7265	
Hγ	4430–4740	4425–4755
Hβ	4810–5410	4755–5420
Hβ_{blue}+He II λ4686	4810–4960	4755–5420
Hβ_{center}	4960–5175	4755–5420
Hβ_{red}	5175–5410	4755–5420
He I λ5876$_{center}$	5980–6270	5755–6530
Hα	6540–7245	6530–7255
Hα_{blue}	6540–6740	6530–7255
Hα_{center}	6740–7000	6530–7255
Hα_{red}	7000–7245	6530–7255

Notes. The continuum wavelength values in brackets correspond to the rest frame of Mrk 926. All wavelengths are given in Å.

Table 3. Observed narrow-emission-line fluxes as measured in the mean spectrum shown in Fig. 3.

Line	Flux	Line	Flux
Hγ_{narrow}	7.4 ± 1.0	[O I] λ6363	8.0 ± 1.5
He II λ4686	6.3 ± 0.9	[N II] λ6548	18.8 ± 3.0
Hβ_{narrow}	15.7 ± 1.8	Hα_{narrow}	42.4 ± 3.4
[O III] λ4959	102. ± 2.1	[N II] λ6584	54.0 ± 3.4
[O III] λ5007	314. ± 3.3	[S II] λ6717	41.1 ± 2.1
He I λ5876	3.1 ± 0.7	[S II] λ6731	37.0 ± 2.0
[O I] λ6300	33.8 ± 2.7		

Notes. In units of 10^{-15} erg cm^{-2} s^{-1}.

between the wavelength boundaries given in Table 2. The red wing of the He II λ4686 line and the blue wing of Hβ are superimposed because of their very broad line widths. There is no clear minimum between the two lines. Therefore, we assigned the emission-line flux shortward of 4960 Å to a mix of the He II λ4686 line and blue Hβ wing, and the flux longward of 4960 Å to Hβ. Before integrating the emission-line flux, we subtracted a linear pseudo-continuum defined by the continua given in Table 2 (Col. 3). The results of the continuum and the integrated line intensity measurements – including the narrow-line components – are given in Tables B.1 and B.2. For further analysis, we also measured the narrow-line components of each broad line in the mean spectrum. The de-blending process of the narrow and broad components in the Balmer and He I λ 5876 lines is described in more detail in Sect. 3.4. The resulting narrow-line fluxes are presented in Table 3.

We present the light curves of the continuum flux densities at 4425, 4755, 5420, 5485, 5744, and 6530 Å (observed frame) in Fig. 4. In order to increase the temporal resolution, we created a combined continuum light curve based on the HET continuum flux densities at 5420 Å and on the photometric V-band contin-

uum light curve obtained at the Wise Observatory. We followed the procedure described in Grier et al. (2012) and Zetzl et al. (2018) by applying a multiplicative scale factor and an additional flux adjustment component to put the Wise Observatory instrumental magnitude light curve on the same scale as the HET continuum light curve in order to correct for different instrumentations, differences in the aperture sizes and therefore different host galaxy contributions, and constant contributions from emission lines within the bandwidth of the V-band filter. The optimal scale factor and flux adjustment component were determined by finding the set of parameters for which the cumulative difference of (nearly) simultaneous spectroscopic and photometric continuum measurements reached its minimum. The resulting combined light curve is given in Table B.4 and shown in Fig. 5. Excluding the first two data points, the time interval between observations amounts to only 1.1 days. For further analysis, we corrected this light curve for Galactic foreground extinction (A_V = 0.113; Schlafly & Finkbeiner 2011) and subtracted the V-band host galaxy contribution (1.35×10^{-15} erg cm^{-2} s^{-1} Å^{-1}; see Sect. 3.2). For comparison, we also show the combined continuum light curve in Figs. 6, A.1, and A.2 showing the light curves of the integrated emission-line fluxes.

3.2. Host galaxy contribution to the optical continuum flux

The observed flux of the variable AGN component is contaminated by the flux contribution of the host galaxy. This contribution is nearly constant for observations taken with identical aperture, and only minor deviations arise due to slight variations from the exact pointing as well as different seeing conditions. However, these effects are taken into account by our error estimates. The overall host galaxy contribution varies from band to band as the stellar component of the host galaxy has a different flux distribution than the AGN component. To estimate the relative contribution of the host galaxy flux, we used the flux variation gradient (FVG) method (Choloniewski 1981; Winkler et al. 1992; Haas et al. 2011; Zetzl et al. 2018). This method allows the varying AGN flux in our aperture to be disentangled from the host galaxy contribution. We took the continuum flux densities at 4425, 5420, and 6530 Å (observed frame) as proxies for B-, V-, and R-band fluxes, respectively, since these continuum ranges are close to the maxima of the B-, V-, and R-filter curves (B-band filter: 4300 Å, V-band filter: 5400 Å, R-band filter: 6100 Å). In this way, we also excluded the contribution of emission lines (see Fig. 2). Figure 7 shows the B versus V and B versus R fluxes (black solid circles) of Mrk 926 based on the HET spectra (aperture: 2 × 2 arcsec). The B, V, and R values in this figure have been corrected for Galactic foreground extinction (A_B = 0.149, A_V = 0.113, A_R = 0.089; Schlafly & Finkbeiner (2011)) and are given in units of mJy. The converted light curves before and after Galactic foreground extinction are given in Table B.3. The blue dashed line in Fig. 7 gives the best linear fit to the B versus V and B versus R fluxes. The red shaded area marks the range of host slopes for nearby AGN as determined by Sakata et al. (2010). The intersection point between the AGN and host galaxy slopes allows the contribution of the host galaxy fluxes in the B, V, and R bands to be determined; the resulting host galaxy contributions in the individual bands are indicated by the dashed black lines.

We derived a B-band host galaxy contribution of 0.76 mJy (mean of 0.56 mJy and 0.96 mJy). The corresponding values are 1.32 mJy for the V band and 2.82 mJy for the R band. By

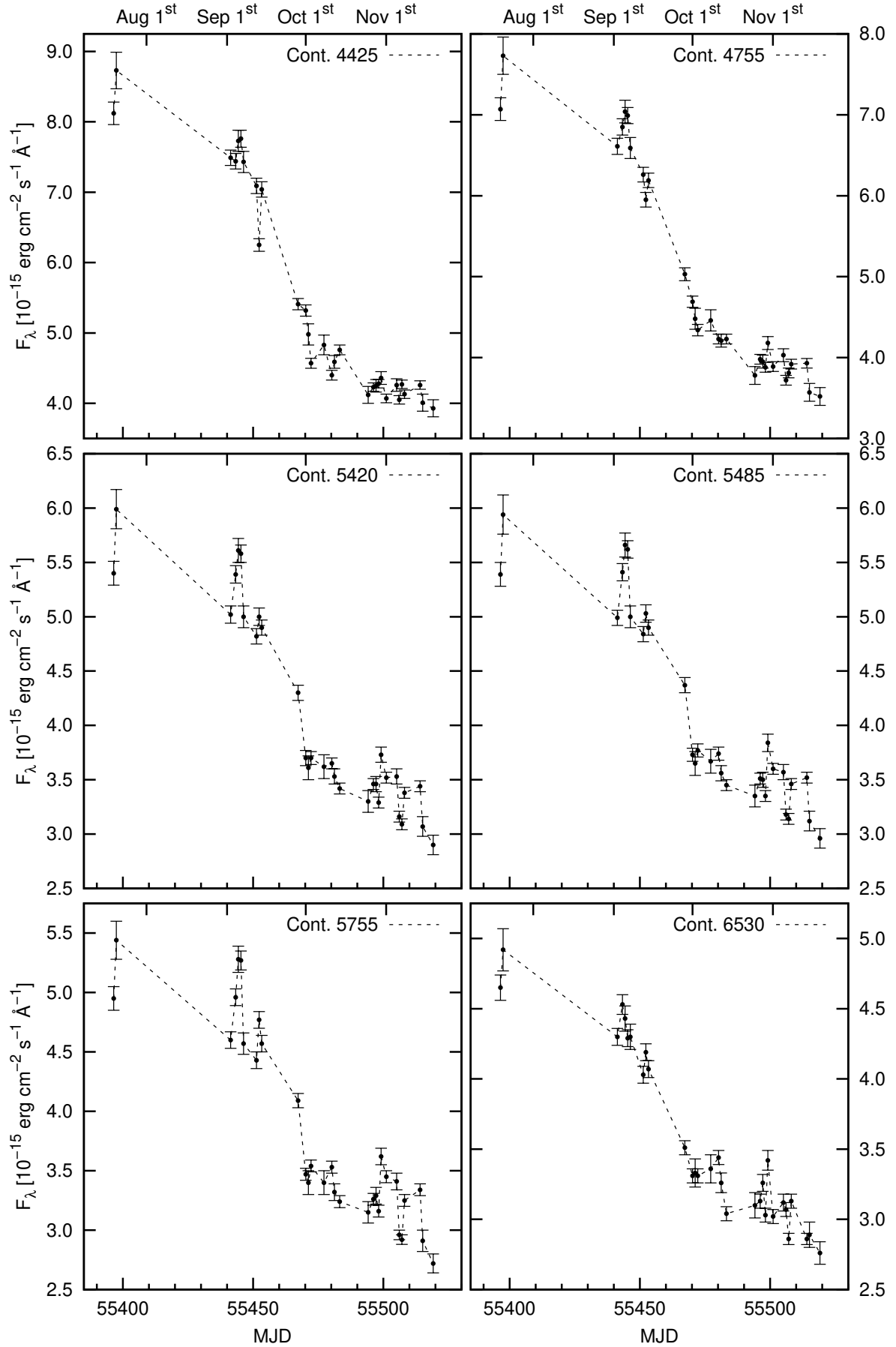**Fig. 4.** Light curves of the continuum flux densities at 4425, 4755, 5420, 5485, 5755, and 6530 Å (observed frame; in units of $10^{-15}\,\mathrm{erg\,cm^{-2}\,s^{-1}\,Å^{-1}}$) of our HET variability campaign from 2010 July 19 to November 19.
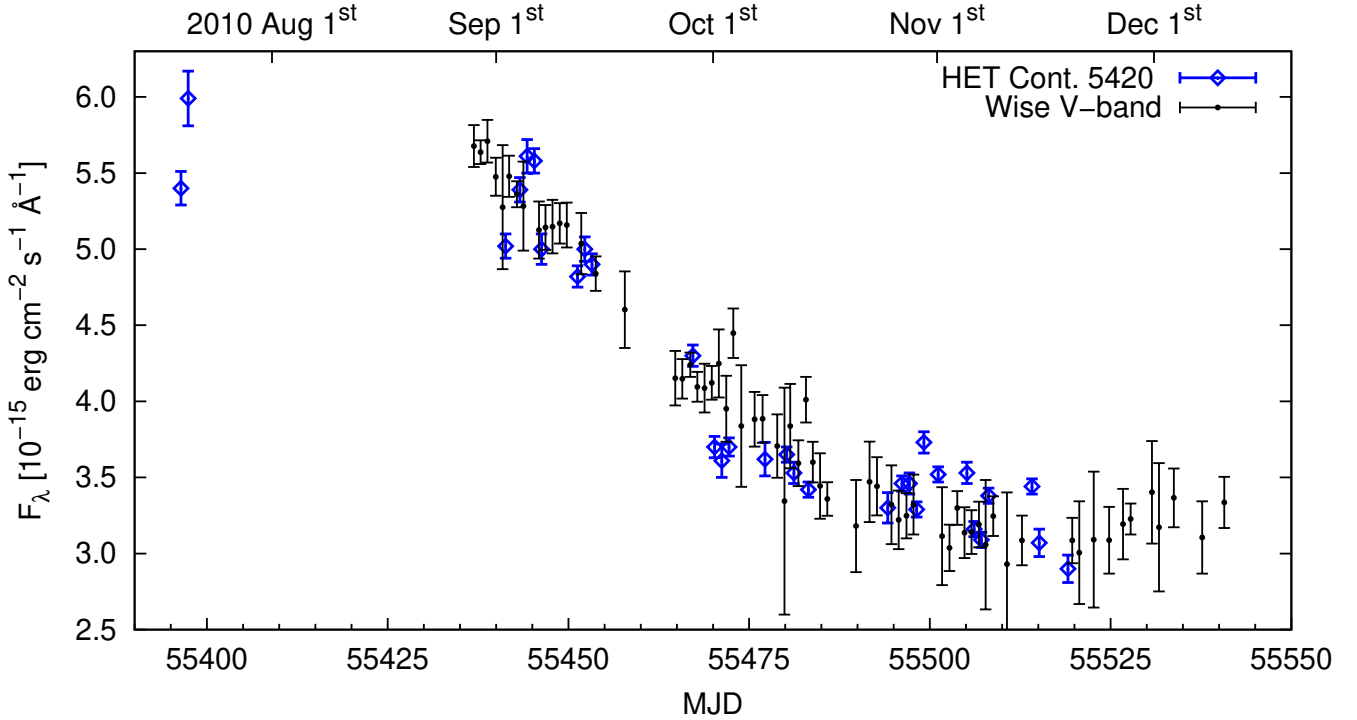
Fig. 5. Combined spectroscopic (HET continuum flux densities at 5420 Å, or 5180 Å in rest frame; blue) and photometric (*V*-band continuum data obtained at the Wise Observatory; black) continuum light curve of our campaign (see Sect. 3.1 for details).

subtracting the host galaxy contribution for each individual band, we isolate the AGN flux in all bands. All flux values (minimal and maximal host+AGN, host contribution as well as true minimal and maximal AGN flux) are listed in Table 4. Based on the HET spectra, the host galaxy contribution corresponds to 12–26 %, 20–42 %, and 37–66 % for the *B*, *V*, and *R* bands, respectively. Altogether, the spectra of Mrk 926 are dominated by emission from the nucleus. The weak host contribution in the *B* and *V* bands and, especially, the very strong and broad emission lines prevent us from subtracting a reliable host galaxy template since the stellar signature of the host galaxy is suppressed.

3.3. Variability statistics

The following statistics are based on the spectroscopic and photometric observations from HET and the Wise Observatory, respectively. The continua were corrected for Galactic foreground extinction (see Sect. 3.1), and the lines were corrected for contribution from the narrow lines (see Table 3). In Table 5, we present the minimum and maximum fluxes, $F_{\min}$ and $F_{\max}$, peak-to-peak amplitudes, $R_{\max} = F_{\max}/F_{\min}$, the mean flux over the period of observations, $\langle F \rangle$, the standard deviation, σ_F, and the fractional variation,

$$F_{\mathrm{var}} = \sqrt{\sigma_F^2 - \Delta^2}/\langle F \rangle, \qquad (1)$$

as defined by Rodríguez-Pascual et al. (1997). The quantity Δ^2 is the mean square value of the uncertainties Δ_i associated with the fluxes F_i. The F_{var} uncertainties are defined in Edelson et al. (2002). The peak-to-peak amplitudes and the fractional variations in the continuum decrease as a function of wavelength.

3.4. Mean and rms line profiles

We determined normalized mean and rms profiles of the Balmer and He I lines in Mrk 926 after subtracting a linear

pseudo-continuum from each mean and rms broad-line profile. In order to obtain the true mean broad-line profiles, we subtracted the narrow Balmer and He I line components in velocity-space by means of a scaled [O III] λ5007 template based on the observed [O III] λ5007 line profile in our mean spectrum. Furthermore, we subtracted the [NII]6548/6584 emission lines that are superimposed on the mean Hα profile using the same template and sticking to a line-ratio of 1:3. The rms profiles illustrate the line profile variations during our campaign. Therefore, the constant narrow components disappear in these rms profiles. Finally, we normalized both the mean and rms profiles such that the maximum line flux was set to unity. The final normalized mean and rms profiles of the Balmer lines Hα, Hβ, Hγ, as well as of the He I λ5876 line in velocity space are shown in Fig. 8. The subtraction of all narrow Balmer and He I components as well as of [NII]6548/6584 and the normalization of the true broad-line profiles allows the mean and rms profiles to be compared with each other in a more accurate way.

The Balmer lines exhibit – besides to their central component – an additional inner red component at $1200 \pm 300 \, \mathrm{km \, s^{-1}}$ in the mean as well as rms profiles (see Fig. 8). Furthermore, the Balmer lines show additional outer broad-line components in their rms profiles (Fig. 8) at ± 5000 to $\pm 13\,000 \, \mathrm{km \, s^{-1}}$. These Balmer satellites are clearly separated from the central component ($\pm 5000 \, \mathrm{km \, s^{-1}}$) and exhibit an amplitude that amounts to 25–40% of that of the maximum rms amplitude in Hα and Hβ, respectively. These components are not recognizable in the mean profiles. The Hγ profile is contaminated by the [OIII] λ4363 line and a strong residual is present in the rms profile. This is due to Hγ being at the blue end of the spectrum where the flux calibration for the first few pixels is not optimal. Furthermore, it is not possible to fix a line-free continuum region on the blue side. These boundary effects heavily affect the blue part of the Hγ line profile. Therefore, the Hγ profile can only be

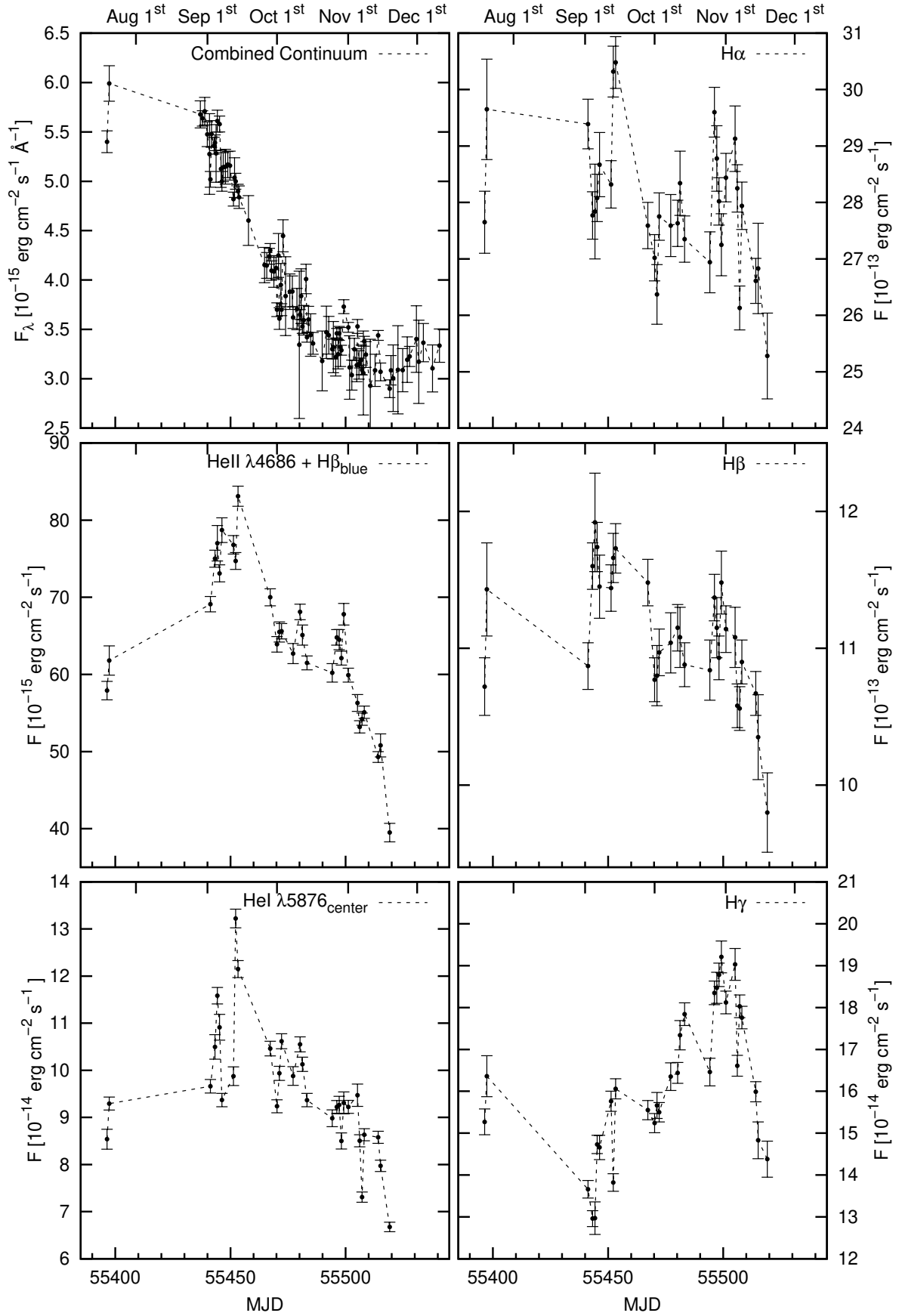**Fig. 6.** Light curves of the combined continuum flux densities at 5420 Å (observed frame; in units of $10^{-15}\,\mathrm{erg\,cm^{-2}\,s^{-1}\,\AA^{-1}}$) as well as of the integrated emission-line fluxes of Hα, Hβ, Hγ, He $\textsc{ii}\,\lambda4686 + \mathrm{H}\beta_{\mathrm{blue}}$, and He $\textsc{i}\,\lambda5876$ for our HET variability campaign from 2010 July 19 to November 19.
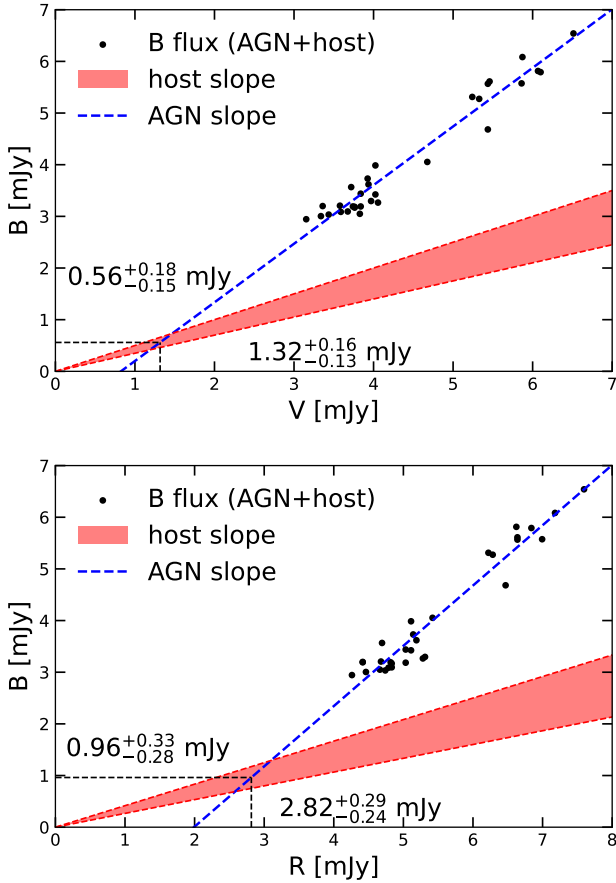
Fig. 7. Extinction-corrected *B* versus *V* (*upper panel*) and *B* versus *R* (*lower panel*) flux variations of Mrk 926. The dashed blue lines (AGN slope) represent the best linear fit to the *B* versus *V* and *B* versus *R* fluxes, respectively. The red shaded area shows the range of host slopes. The dashed black lines indicate the *B* and *V* as well as the *B* and *R* values of the host galaxy.

Table 4. Extinction-corrected *B*, *V*, and *R* values for the combined host galaxy plus AGN fluxes as well as for the host galaxy and AGN fluxes alone as determined by the FVG method.

Flux component	*B* band	*V* band	*R* band
		[mJy]	
(1)	(2)	(3)	(4)
Host+AGN (BvsR)	2.94–6.54		4.26–7.60
Host+AGN (BvsV)	2.94–6.54	3.15–6.51	
Host (BvsR)	0.96		2.82
Host (BvsV)	0.56	1.32	
AGN (BvsR)	1.98–5.58		1.44–4.78
AGN (BvsV)	2.39–5.98	1.83–5.19	
		$[10^{-15}\,\mathrm{erg\,s^{-1}\,cm^{-2}\,\AA^{-1}}]$	
(1)	(2)	(3)	(4)
Host+AGN (BvsR)	4.51–10.01		3.00–5.34
Host+AGN (BvsV)	4.51–10.01	3.22–6.65	
Host (BvsR)	1.47		1.98
Host (BvsV)	0.86	1.35	
AGN (BvsR)	3.03–8.54		1.01–3.36
AGN (BvsV)	3.66–9.16	1.87–5.30	

Notes. When a range is given, it corresponds to the minimum and maximum flux.

Table 5. Variability statistics ($F_{\min}$, $F_{\max}$, $R_{\max}$, $\langle F \rangle$, σ_F, and F_{var}) for the continuum (after correction for Galactic foreground extinction) and for the broad emission lines (after correction for the contribution of narrow-line components; see Table 3).

Cont./Line	$F_{\min}$	$F_{\max}$	$R_{\max}$	$\langle F \rangle$	σ_F	F_{var}
Comb. *V* band	3.22	6.65	2.07	4.41	0.97	0.21
Cont. 4425 (4225)	4.51	10.01	2.22	6.22	1.77	0.28
Cont. 4755 (4540)	4.04	8.87	2.20	5.67	1.52	0.27
Cont. 5420 (5180)	3.22	6.65	2.07	4.50	1.01	0.22
Cont. 5485 (5240)	3.28	6.59	2.01	4.54	0.99	0.22
Cont. 5755 (5500)	3.02	6.04	2.00	4.23	0.90	0.21
Cont. 6530 (6240)	3.00	5.34	1.78	3.85	0.68	0.17
Cont. 7255 (6930)	3.20	5.03	1.57	3.93	0.54	0.14
Hγ	122.2	184.7	1.51	154.6	17.6	0.11
Hβ	542.	754.	1.39	670.	46.	0.07
Hβ_{blue}+He II λ4686	33.2	76.80	2.31	57.8	9.6	0.17
Hβ_{center}	419.	556.	1.33	502.	30.	0.06
Hβ_{red}	89.2	126.8	1.42	109.5	8.5	0.08
HeI λ5876$_{\mathrm{center}}$	63.7	129.1	2.03	92.7	13.2	0.14
Hα	2293.	2813.	1.23	2562.	118.	0.04
Hα_{blue}	131.3	192.4	1.47	159.2	14.7	0.09
Hα_{center}	2082.	2456.	1.18	2286.	93.3	0.04
Hα_{red}	79.6	166.9	2.10	116.1	23.9	0.21

Notes. In units of $10^{-15}\,\mathrm{erg\,s^{-1}\,cm^{-2}\,\AA^{-1}}$ for the continuum and in units of $10^{-15}\,\mathrm{erg\,s^{-1}\,cm^{-2}}$ for the broad emission lines. The fluxes in this table are observed-frame fluxes. The continuum wavelength values in brackets correspond to the rest frame of Mrk 926.

used to derive some general trends. Despite the boundary effects mentioned before, the rms profile of Hγ confirms the presence of Balmer satellites at ± 5000 to $\pm 13\,000\,\mathrm{km\,s^{-1}}$. The red wing of He I λ5876 might also indicate the presence of such a line satellite, however, a clear detection cannot be stated due to the interference by absorption in the line wings. In addition, the central He I λ5876 profile is contaminated by NaD absorption.

We determined the line widths (FWHM) of the mean and rms line profiles of all the Balmer lines and He I λ5876. Additionally, we parameterized the line widths of the mean profiles by their line dispersion σ_{line} (Fromerth & Melia 2000; Peterson et al. 2004). However, due to the very broad, partially overlapping and complex rms line profiles with additional outer components, it was not possible do determine reliable σ_{line} (rms) values. Likewise, by cause of Hγ being affected by boundary effects, the overlapping He II λ4686 and Hβ_{blue} profiles, as well as strong absorption in He I λ5876, a determination of σ_{line} (mean) for these lines was deemed unreliable. Therefore, we determined the line dispersion σ_{line} (mean) solely for the Hα mean profile over a velocity interval from $-15\,000$ to $+15\,000\,\mathrm{km\,s^{-1}}$.

The resulting widths (FWHM) for all emission lines, and the line dispersion of Hα ($\sim 3500\,\mathrm{km\,s^{-1}}$) are given in Table 6. The Hα and Hβ lines show similar mean profiles with line widths

(FWHM) of $\sim 5200\,\mathrm{km\,s^{-1}}$ as well as similar rms profiles with line widths (FWHM) of $\sim 4000\,\mathrm{km\,s^{-1}}$. The H$\gamma$ line exhibits a profile similar to that of Hα and Hβ, but the line width and line dispersion are smaller than for the other Balmer lines. We note, however, that these results are less reliable due to the aforementioned boundary effects. The He I λ5876 line (mean and rms) is by a factor of about 1.5 broader than the Balmer lines.

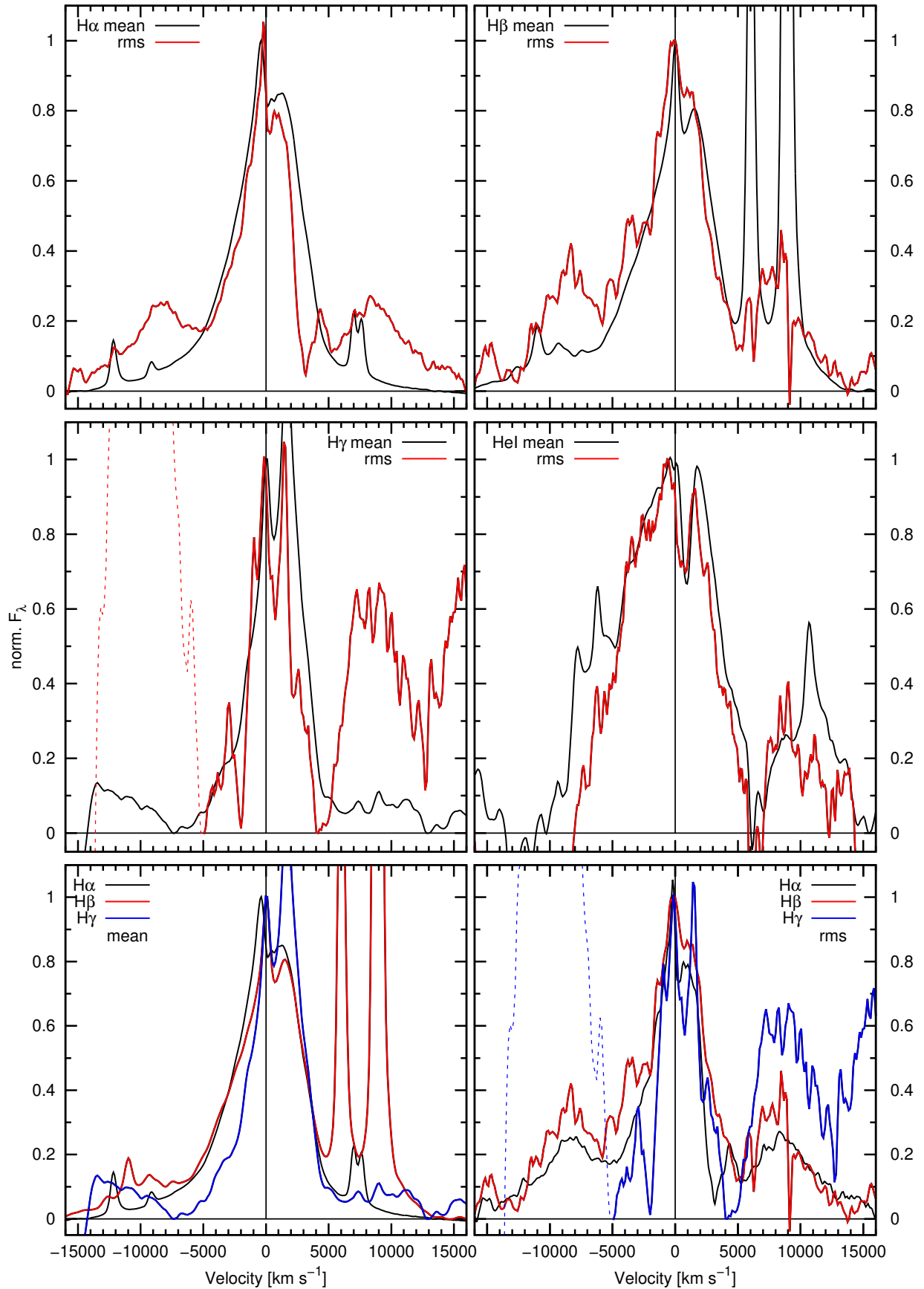**Fig. 8.** Normalized mean and rms profiles of the Balmer lines and HeI λ5876 in velocity space. The dashed part of the Hγ line profile denotes the part that is heavily affected by uncertainties in the flux calibration due to boundary effects at the blue end of the spectrum.

3.5. CCF analysis of the broad emission lines

The mean distances of the broad emission-line regions to the central ionizing source can be determined by correlating the broad emission-line light curves with the light curve of the ionizing continuum flux. Normally, an optical continuum light curve is used as surrogate for the ionizing light curve. For this study, we correlated the integrated light curves as well as the segment light curves (center, blue, red) of the Balmer lines Hα and Hβ, and the He I $\lambda5876_{\text{center}}$ line with the combined 5180 Å (rest frame) and V-band continuum light curve (see Fig. 5 in Sect. 3.1). For Hγ, the boundary effects mentioned in Sect. 3.4 prevented a reliable light curve extraction, and therefore no cross-correlation function (CCF) was calculated. The correlation technique we used is a variant of the discrete correlation function (DCF; Edelson & Krolik 1988). Instead of classically binning the data points (i.e., using a rectangular weighting function), we performed a weighted averaging of the data points using a Gaussian kernel $b_\tau(t) = (1/\sqrt{2\pi h}) \exp(-(\tau - t)^2/2h^2)$ as a smooth density function (Rehfeld et al. 2011, and references therein). The width h was chosen such that it was on the order of the mean sampling rate, which in our case translates to ~2 days. The Pearson correlation coefficient, $\rho_{x,y} = \text{COV}(x, y)/(\sigma_x\sigma_y)$, of two time series, x and y, with time steps t^x and t^y then transforms to

$$\text{CCF}(\tau) = \frac{\sum_{i=1}^{N_x}(x_i - \mu_x) \cdot (z_i^\tau - \mu_{z^\tau})}{N_x \sigma_x \sigma_z}, \tag{2}$$

with $z_i^\tau = \sum_{j=1}^{N_y} y_j \cdot b_\tau(t_j^y - t_i^x)$. The normalization of the CCF ensures that $\text{CCF}(\tau) \leq 1$ for all τ. We note that the light curves were not detrended as the timescale of the campaign does not suffice to remove long-term trends. The derived cross-correlation functions, $\text{CCF}(\tau)$, are shown in Fig. 9.

We determined the centroids τ_{cent} of the CCFs by using only those parts of the CCFs above 80% of the peak value. A threshold value of 0.8 r_{max} is generally a good choice as has been shown before (Peterson et al. 2004). We derive the uncertainties of the time lags, τ_{cent}, by calculating the cross-correlation lags a large number of times using a model-independent Monte Carlo method known as flux randomization/random subset selection (FR/RSS). This method has been described by Peterson et al. (1998). The resulting cross-correlation centroid distributions (CCCDs) for the integrated Hα, Hβ, and He I lines as well as for their line segments (center, blue, red) with the combined 5180 Å (rest frame) and V-band continuum are presented in Fig. 9. Each CCCD was determined after 2×10^4 independent runs (i.e., 2×10^4 independent subsamples) for each light curve. For the CCFs of the central Balmer line segments showing two distinct peaks, the CCCD was calculated for each peak individually. The final centroid time lags are given in Table 7. The error intervals correspond to 68% ($\pm1\sigma$) confidence level.

The resulting CCFs and CCCDs are presented in Fig. 9. The CCFs of the integrated Balmer line light curves and of the central Balmer line component light curves (within ±5000 km s^{-1}) exhibit two discrete peaks. In contrast, the blue and red Balmer segment light curves (i.e., the light curves of the Balmer satellites) are single-peaked. The double-peaked CCFs of the integrated Balmer line light curves show delays of 8^{+2}_{-5} and 56^{+3}_{-6} days for Hα, and 5^{+2}_{-2} and 48^{+9}_{-6} days for Hβ. The CCFs of the central Balmer line component light curves show delays of 10^{+3}_{-2} and 57^{+3}_{-3} days for Hα, and 5^{+2}_{-2} and 48^{+7}_{-6} days for Hβ. The interpretation of these double-peaked CCFs is explained in more detail in Sect. 3.6. The CCFs of the Balmer satellite light curves are

Table 6. FWHM of the mean and rms line profiles as well as the line dispersion, σ_{line}, of the mean profiles.

Line	*FWHM* (mean) [km s^{-1}]	*FWHM* (rms) [km s^{-1}]	σ_{line} (mean) [km s^{-1}]
Hα	5370 ± 400	3890 ± 500	3460 ± 1000
Hβ	5110 ± 400	4230 ± 400	–
Hγ	4300 ± 1000	3260 ± 800	–
He I $\lambda5876$	8500 ± 1000	7650 ± 800	–

single-peaked and show, in comparison to the CCFs of the integrated and central component light curves, much shorter delays of only 3−5 light-days (i.e., the Balmer satellites react promptly to the variations in the continuum). There are indications for a secondary peak in the red Balmer satellite CCF of Hβ (see Fig. 9c); however, the light curve of this wing is relatively noisy due to the strong underlying [O III] lines (see Sect. 4.5.2 for more information). The CCF of the blue Hβ Balmer satellite shows no indication of a secondary peak.

We also calculated the CCFs and CCCDs for the weak HeI $\lambda5876$ line. The outer wings are heavily contaminated by absorption. Therefore, out of precaution we excluded the blue and red wing from the integrated line light curve, leaving only the central profile light curve. In contrast to the Balmer lines, the CCF of the central profile light curve only shows a singular peak at a delay of 7^{+4}_{-2} days and no evidence for a secondary peak. Instead, the singular peak is very broad and high correlation values are found for delays up to ~40 days.

The overall lags determined by the CCF analysis do not depend significantly on the use of either the purely spectroscopic or the combined spectroscopic and photometric continuum light curve. Both driving light curves recover the same responses of the emission lines with only minor variations of ±2 days at maximum. In comparison to the spectroscopic driving light curve, the use of the combined continuum light curve generates more stable CCFs and narrower, more confined CCCDs.

3.6. Velocity-resolved CCFs of the Hα and Hβ line

In Sect. 3.5 we calculated the time lags of the integrated Hα, Hβ, and HeI lines as well as of the central and outer wing regions with respect to the combined V-band continuum at 5180 Å (rest frame). Now, we investigate the profile variations in the Hα and Hβ lines in more detail by calculating the lags of individual line segments. For the weak HeI $\lambda5876$ line, the absorption in the central line segment and in the line wings prohibits a clear determination of a velocity-resolved CCF. The way we proceed has been described before in our studies of line profile variations in Mrk 110 (Kollatschny & Bischoff 2002; Kollatschny 2003), Mrk 926 (Kollatschny & Zetzl 2010), 3C120 (Kollatschny et al. 2014) and HE 1136-2304 (Kollatschny et al. 2018).

We sliced the velocity profiles of the continuum-subtracted Balmer lines into velocity segments with a width of $\Delta v = 400$ km s^{-1}. This value of 400 km s^{-1} corresponds to the spectral resolution of our observations. A central line-segment was integrated from $v = -200$ to $+200$ km s^{-1}. Afterward, we measured the intensities of all subsequent line-of-sight velocity segments from $v = -15\,800$ to $+15\,800$ km s^{-1} and compiled their light curves. We computed the CCF(τ) for each individual line-segment light curve ($\Delta v = 400$ km s^{-1}) of Hα and Hβ with respect to the combined 5180 Å (rest frame) continuum light
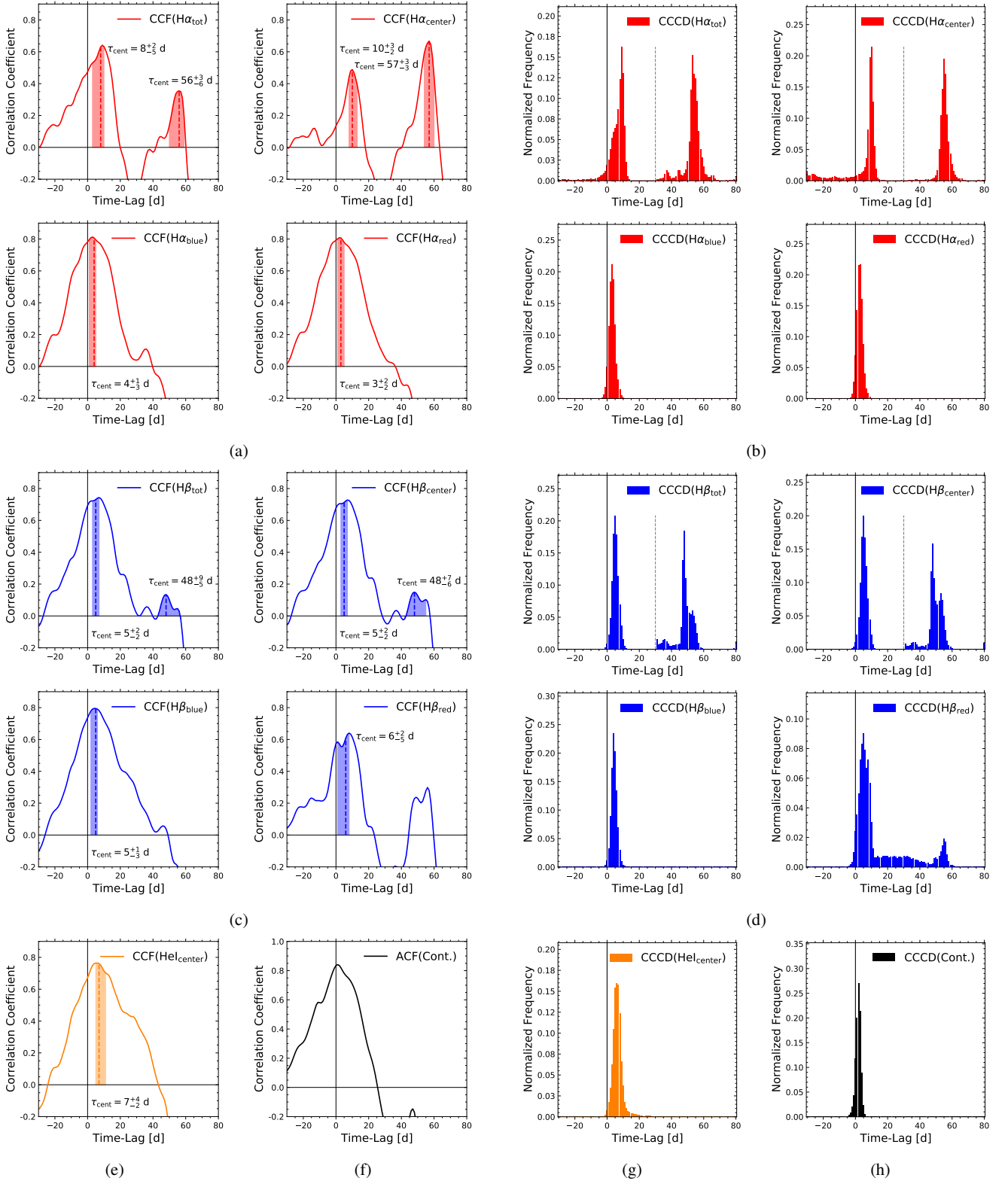
Fig. 9. *Left panel*: CCFs of the integrated Hα *(a)* and Hβ *(c)* line, of their segments (center, blue, red), and of the central He I line *(e)* with respect to the combined continuum at 5180 Å (rest frame). The time lag, τ_{cent}, is denoted by a dashed line, with the shaded area corresponding to a $\pm 1\sigma$ interval. The CCF of the spectroscopic continuum light curve with respect to the combined (photometric plus spectroscopic) continuum reference light curve is shown in *(f)*. *Right panel*: CCCDs of the integrated Hα *(b)* and Hβ *(d)* line, of their segments (center, blue, red), and of the central He I line *(g)* with respect to the combined continuum at 5180 Å (rest frame). The boundary between CCCDs of individual peaks is denoted by a dashed gray line. The CCCD of the spectroscopic continuum light curve with respect to the combined continuum reference light curve is shown in *(h)*.

Table 7. Cross-correlation lags of the integrated Hα and Hβ line light curves as well as of their line segments (center, blue, red) with respect to the combined 5180 Å (rest frame) and *V*-band continuum light curve.

	Line					
	Hα τ [days]		Hβ τ [days]		He I τ [days]	
Segment	Inner	Outer	Inner	Outer	Inner	Outer
Total	8^{+2}_{-5}	56^{+3}_{-6}	5^{+2}_{-2}	48^{+9}_{-5}	–	–
Center	10^{+3}_{-2}	57^{+3}_{-3}	5^{+2}_{-2}	48^{+7}_{-6}	7^{+4}_{-2}	–
Blue	4^{+1}_{-3}	–	5^{+1}_{-3}	–	–	–
Red	3^{+2}_{-2}	–	6^{+2}_{-5}	–	–	–

curve. In this way, we computed velocity-resolved CCFs of Hα and Hβ as a function of distance to the line center (blue scale). These velocity-resolved CCFs are shown in Figs. 10a and b. The green lines in these figures delineate the contour lines of the correlation coefficient at different levels (0.2, 0.4, 0.5, 0.6, 0.7, 0.75, 0.8, 0.825). The red line shows the rms line profile for comparison.

The Hα line shows two velocity-delay structures in the central segment (within ± 5000 km s^{-1}) at a distance of 57^{+3}_{-3} and 10^{+3}_{-2} light-days (see Sect. 3.5). Adopting the interpretation of Horne et al. (2021) for the velocity-delay maps of the NGC 5548 STORM campaign, this structure might be interpreted as the upper and lower half of an ellipse in the velocity-delay plane that might be the signature of a line-emitting ring orbiting the black hole (BH) at a radius $R = 33.5$ light-days. The stronger far side of the annulus extends to $\tau = (R/c)\,(1 + \sin i) \approx 57$ days, and the weaker near side of the annulus has a delay of $\tau = (R/c)\,(1 - \sin i) \approx 10$ days. This gives $\sin i \sim 0.71$ and thus $i \sim 45°$ as the inclination angle of an assumed thin disk.

The Hβ line also shows two velocity-delay structures in the central segment at 48^{+7}_{-6} and 5^{+2}_{-2} light-days (see Sect. 3.5). A possible line-emitting ring orbiting the BH therefore has a radius $R = 26.5$ light-days. The weaker far side of the annulus then extends to $\tau = (R/c)\,(1 + \sin i) \approx 48$ days, and the stronger near side of the annulus has a delay at $\tau = (R/c)\,(1 - \sin i) \approx 5$ days. This gives $\sin i \sim 0.81$ and thus $i \sim 54°$ of the disk. Therefore, we adopt $i \sim 50°$ as the mean disk inclination angle.

3.7. Central black hole mass

The masses of the central BHs in AGN can be estimated – based on the assumption that the gas dynamics are dominated by the central massive object – by evaluating

$$M = f\,c\,\tau\,\Delta v^2\,G^{-1}. \tag{3}$$

The characteristic velocity Δv of the emission-line region can be estimated from the FWHM of the rms profiles or from the line dispersions σ_{line}. Furthermore, the distance $c\,\tau$ of the line-emitting regions from the ionizing source can be estimated from the delayed response of the line light curves to the continuum variations. Characteristic distances of the individual line-emitting regions are given by the centroid τ_{cent} of the individual CCFs of the emission-line variations relative to the continuum variations (e.g., Koratkar & Gaskell 1991; Kollatschny & Dietrich 1997).

The scaling factor f in Eq. (3) is on the order of unity and depends on the kinematics, structure, and orientation of the

BLR. This scaling factor differs by ~0.4 dex rms from galaxy to galaxy, for example, depending on whether we see the central accretion disk including the BLR from the edge or face-on. Typically, the scaling factor f is discussed with respect to the line dispersion σ_{line} (rms). Empirically found f values are $f = 5.5$ (e.g., Onken et al. 2004), $f = 4.31$ (e.g., Grier et al. 2013a), or $f = 3.6$ (Graham et al. 2011). The very broad lines in Mrk 926 (see Sect. 3.4) and the high disk inclination angle of $i \sim 50°$ (see Sect. 3.6) indicate that Mrk 926's orientation toward us is rather edge-on in comparison to other AGN. Therefore, we adopt an f value of $f = 3.6$ in order to calculate the BH mass. We note that the virial factor, f, for σ_{line} and FWHM differs since $FWHM/\sigma_{\mathrm{line}}$ typically takes values of ~2 (Peterson et al. 2004). We account for that by following the procedure in Kollatschny & Zetzl (2011, 2013) and, for example, Kollatschny et al. (2018): adopting a correction factor in order to obtain the true rotational velocity, v, from the observed FWHM for each line. This reduces the effective f factor of FWHM to ~1.2. We use FWHM (rms), which generally gives more reliable results than FWHM (mean) due to the fact that the rms profiles only shows the varying fraction of the BLR line-emitting gas. Based on the delays of the central Balmer line regions (see Table 7 and Sect. 3.6) and on the line widths of the rms profiles (FWHM) (see Table 6), we derive a weighted mean BH mass (see Table 8) of

$$M = (1.1 \pm 0.2) \times 10^8\,M_\odot \ \text{ or } \ \log(M/M_\odot) = 8.04 \pm 0.1. \tag{4}$$

The BH mass based on the HeI $\lambda 5876$ line has a larger error due to larger uncertainties in their FWHM. However, it confirms the BH mass derived from the Balmer lines. The BH mass estimate based on the Hα line dispersion σ_{line} (mean) is by a factor of ~2 larger than the BH estimate from the FWHM (rms). Considering the larger uncertainties of σ_{line}, it is still in agreement with the BH mass estimates from FWHM (rms).

4. Discussion

4.1. Optical variability

4.1.1. Optical variability amplitudes

It is known that Mrk 926 varied at least since the beginning of the 1990s (Kollatschny et al. 2006). A first variability campaign was carried out during the years 2004–2005 (Kollatschny & Zetzl 2010). Back then, the optical continuum flux density at 5180 Å varied between 2.4 and 3.6 $\times 10^{-15}$ erg cm^{-2} s^{-1} Å^{-1}. In July 2010, the continuum flux density was significantly higher and amounted to a value of 6×10^{-15} erg cm^{-2} s^{-1} Å^{-1} at 5180 Å (rest frame) at the beginning of the variability campaign presented here. Immediately afterward, the optical continuum started to drop, finally reaching less than 50% of its original intensity (see Fig. 5 and Table B.1) within only 2.5 months. Even more remarkably, the true non-stellar continuum in Mrk 926 declines to only 30–40% continuum intensity between the beginning and end of the variability campaign taking into account the constant host galaxy contribution to the flux as determined by means of the FVG method (see Table 4).

The variability amplitude in the blue spectral range is higher than in the red (see Table 5 and the rms spectrum in Fig. 3). Interestingly, the continuum variation amplitudes in Mrk 926 are much higher than those observed in other highly variable and even changing-look AGN. For example, during a post-outburst campaign in 2014-2015, the changing-look AGN HE 1136-2304
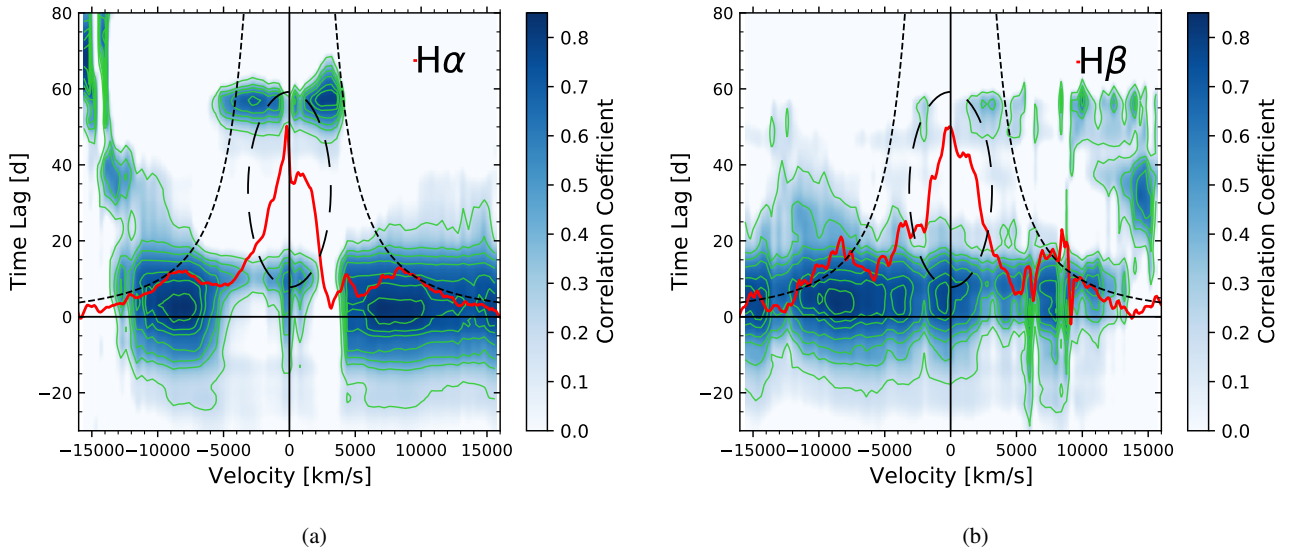
(a)

(b)

Fig. 10. Velocity-resolved CCFs(τ, v) showing the correlation coefficient of the Hα *(a)* and Hβ *(b)* line segment light curves ($\Delta v \sim 400\,\mathrm{km\,s^{-1}}$) with respect to the combined continuum light curve as a function of velocity and time delay (blue scale). Contours of the correlation coefficients are plotted at levels 0.2, 0.4, 0.5, 0.6, 0.7, 0.75, 0.8, and 0.825 (green lines). In each plot, the rms profile of the emission line is shown in red. The dashed curve shows the escape velocities for a Keplerian disk inclined by $\sim$50° with a central mass of $1.1 \times 10^8 M_\odot$. The dashed ellipse corresponds to a circular Keplerian orbit at $R/c = 33.5$ d inclined by $\sim$50° to the line of sight mapped onto the velocity-delay plane. The line center ($v = 0\,\mathrm{km\,s^{-1}}$) and the time delay of $\tau = 0$ days are indicated by a vertical and a horizontal black line, respectively. The delays computed for the red wing of Hβ are disturbed by the [O III] λ 4959, 5007 lines, which results in higher-delay residuals not confined within the viral envelope.

Table 8. Black hole masses based on the FWHM of the line profiles in the rms spectra and the line dispersion σ_{line} of the mean Hα profile.

Line	$M_{\mathrm{BH},FWHM}$ [$10^8 M_\odot$]	$M_{\mathrm{BH},\sigma_{\mathrm{line}}}$ [$10^8 M_\odot$]
Hα	1.2 ± 0.4	2.8 ± 1.7
Hβ	1.1 ± 0.3	–
Weigh. mean	1.1 ± 0.2	–
HeI λ5876	1.0 ± 0.6	–

Notes. The masses were calculated assuming an f value of 3.6.

exhibited a fractional variation of $F_{V,\mathrm{var}} = 0.11$ and $F_{V,\mathrm{var}} = 0.25$ with and without host, respectively (Zetzl et al. 2018). Mrk 926 exhibits fractional variation of $F_{V,\mathrm{var}} = 0.22$ and $F_{V,\mathrm{var}} = 0.31$ with and without host, respectively. The fractional variation depends on the duration of the monitoring campaign, on the examined wavelength, and on the (accurate) subtraction of the host galaxy contribution. A typical value for the fractional variation $F_{V,\mathrm{var}}$ of the continuum at roughly 5100 Å is 0.05–0.15 for variability periods of 6–12 months. For longer campaigns, typical $F_{V,\mathrm{var}}$ values are higher and range from 0.1 to 0.25 (Zetzl et al. 2018, and references therein). On timescales of years, a decline of the continuum to only 20% of its original value has been observed for some sources (e.g., Fairall 9; Kollatschny & Fricke 1985). However, Mrk 926 was observed for a much shorter period and showed a similarly drastic decline. To summarize, it can be stated that the optical continuum variations in Mrk 926 are very strong.

4.1.2. Signature of an accretion disk in Mrk 926

We now intend to test whether the observed continuum spectral index in the optical is consistent with theoretical predic-
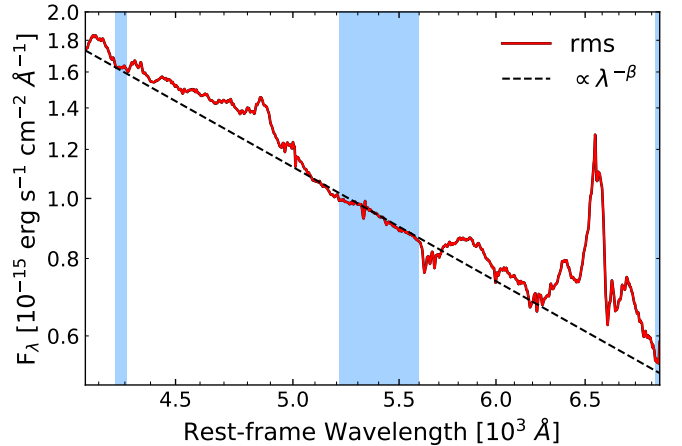

Fig. 11. RMS spectrum of the HET campaign corrected for Galactic foreground extinction. A power-law model was fitted to the continuum, giving a spectral index $\beta = 2.33 \pm 0.02$.

tions from the Shakura & Sunyaev accretion disk model (SS73; Shakura & Sunyaev 1973). Specifically, the Shakura & Sunyaev model predicts $f_\nu \propto \nu^{1/3}$ over the self-similar part of the spectrum, that is, far away from the spectral bands affected by the inner (UV to extreme UV) and outer (far-infrared) disk radii. This holds for Mrk 926 over the optical range. The spectral index of $\alpha = 1/3$ for f_ν then translates to $\beta = -7/3$ for f_λ as $f_\lambda = f_\nu \mathrm{d}\nu/\mathrm{d}\lambda \sim \nu^{1/3}\nu^2 \sim \lambda^{-7/3}$.

Figure 11 shows the observed rms spectrum corrected for Galactic foreground extinction. A power-law model $F_\lambda \propto \lambda^{-\beta}$ was fitted to the continuum (blue shaded areas), giving a spectral index $\beta = 2.33 \pm 0.02$. The rms spectrum of the continuum is thus consistent with a power-law with a spectral index of $\beta = 7/3$ as predicted by the Shakura & Sunyaev model.
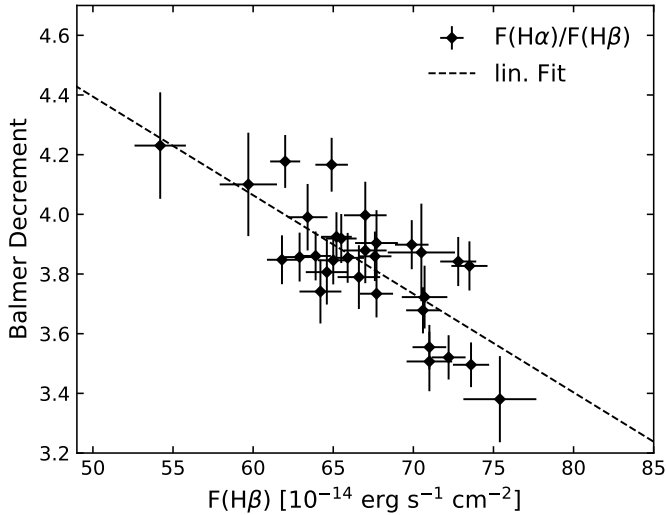
Fig. 12. Balmer decrement, $F(H\alpha)/F(H\beta)$, of the broad-line components versus broad-line $H\beta$ intensity. The dashed line on the graph represents the linear regression.

4.1.3. Balmer decrement variability

The Balmer decrement $F(H\alpha_{\text{narrow}})/F(H\beta_{\text{narrow}})$ of the narrow-line components in Mrk 926 amounts to 2.70 (see Table 3). This corresponds to the expected theoretical line ratio (Case B) without any reddening. The lack of reddening toward the narrow-line region (NLR) is consistent with the insignificant reddening implied by the RMS fit to a Shakura & Sunyaev model (see Sect. 4.1.2). In contrast to the constant Balmer decrement of the narrow lines, the Balmer decrement of the broad-line components takes values of 3.4–4.2. Figure 12 shows the Balmer decrement $F(H\alpha_{\text{broad}})/F(H\beta_{\text{broad}})$ versus broad-line $H\beta$ flux.

The Balmer decrement varies as a function of the broad $H\beta$ flux. More precisely, the Balmer decrement shows a roughly linear dependence on the $H\beta$ flux, and increases with decreasing $H\beta$ broad-line intensity. Similar, although even stronger variations in the Balmer decrement have been found before in highly variable Seyfert galaxies as, for example, NGC 7603 (Kollatschny et al. 2000) or HE 1136-2304 (Kollatschny et al. 2018). The broad-line Balmer decrement in these galaxies increased up to values of 7.3 in combination with decreasing $H\beta$ line intensities. These observations might be explained by optical depth effects in the BLR. This is in accordance with the finding that $H\alpha$ often originates at larger distances than $H\beta$. It has been discussed by Korista & Goad (2004) that the radial stratification in the BLR is a result of optical-depth effects of the Balmer lines: the broad-line Balmer decrement decreases in high continuum states and increases in low states.

4.2. $H\beta$ lag versus optical continuum luminosity

Now, we test whether Mrk 926 follows the general trend of the $H\beta$-lag and optical continuum luminosity relationship (R_{BLR}–L_{AGN}) for AGN (e.g., Kaspi et al. 2000; Bentz et al. 2013; Kilerci Eser et al. 2015; Grier et al. 2017; Kollatschny et al. 2018, and references therein). We determined continuum luminosities $\log(\lambda L_\lambda/\text{erg s}^{-1})$ of 43.68–44.13 (1.87–5.30 $\times$ 10^{-15} erg s^{-1} cm^{-2} Å^{-1}) in the optical at 5180 Å (rest frame) after correction for the contribution of the host galaxy. Furthermore, we derived a mean distance of 26.5 light-days for the $H\beta$ line-emitting region based on the delay of the $H\beta$ line variability

with respect to the optical continuum light curve. This derived distance of 26.5 light-days for the $H\beta$ line-emitting region and the observed continuum luminosities closely follows the general R_{BLR}–L_{AGN} relation with a slope of $\alpha \sim 0.53$ (Bentz et al. 2013).

4.3. Line profiles

4.3.1. Mean and rms line profiles of the 2010 campaign

The mean and rms profiles of the Balmer and He I $\lambda 5876$ lines in velocity space are presented in Fig. 8. The mean and rms profiles of $H\alpha$ and $H\beta$ are very similar. They exhibit line widths (FWHM) of ~5250 km s^{-1} (mean profiles) and line widths of ~4000 km s^{-1} (rms profiles) (see Table 6). These values are larger than the average. The $H\alpha$ FWHM distribution for broad-line quasars – based on many thousand emission-line galaxies from the Sloan Digital Sky Survey – shows a clear maximum at about 2000 km s^{-1} and falls steadily to FWHM values of about 9000 km s^{-1} (Hao et al. 2005). There is an additional inner red emission component to be seen at $\sim +1500$ km s^{-1}. Such inner red components have been seen before in other variable AGN, for example Ark 120 (Kollatschny et al. 1981), NGC4593 (Kollatschny & Dietrich 1997), NGC7603 (Kollatschny et al. 2000), or HE 1136-2304 (Kollatschny et al. 2018). Possible explanations for these red components might be disk components, additional radial motions, or opacity components. More comments regarding inner red line components can be found, for example, in Gaskell & Harrington (2018) or Du et al. (2018).

The Balmer lines show symmetric additional outer-line components between ± 5000 and $\pm 13\,000$ km s^{-1}, which we term Balmer satellites. We note that the red wing of He I $\lambda 5876$ might also indicate the presence of such a line satellite; however, due to the interference by absorption, a clear detection cannot be claimed. In particular, the Balmer satellites components show up in the rms profiles and their relative variability amplitudes are stronger than that of the central components between -5000 and $+5000$ km s^{-1}. The fractional variations in the individual line components are given in Table 5. Five years before the variability campaign presented here, when Mrk 926 was by 50% fainter in the continuum compared to the beginning of our campaign, these outer components in the rms profiles were also present, but are now slightly more pronounced (Kollatschny & Zetzl 2010). Back in 2005, the central line components were noticeably broader when the source was in a lower state. The central Balmer line components exhibited FWHM rms of roughly 8500 km s^{-1} in 2005 in comparison to 4000 km s^{-1} in 2010. The uncertainties in the line dispersion σ_{line} of the broad emission lines determined in Sect. 3.4 are relatively high. Generally, the line dispersion σ_{line} is very sensitive to the line widths used for integration. However, in Mrk 926, the uncertainties in the line widths – full width at zero intensity (FWZI) – are high because of the large line widths and the additional outer line-components. Therefore, we did not derive a $FWHM/\sigma$ to determine the height/radius ratio of the BLR as presented in other galaxies (e.g., Kollatschny et al. 2018). Typical values for $FWHM/\sigma$ in other galaxies are on the order of two or more. Only in very rare cases the σ_{line} values are equal or larger than the FWHM values (Peterson et al. 2004; Kollatschny & Zetzl 2011, 2013).

4.3.2. Comparison of the 2010 and 2004-2005 campaigns

We now compare the Balmer line profiles observed in 2010 with the Balmer line profiles observed during the campaign in 2004–2005. First, the continuum as well as broad-line flux

in 2005 was by a factor of about two smaller than in 2010 (Kollatschny & Zetzl 2010). Second, the comparison of the Balmer line profiles also reveals differences in the mean and rms profiles. A strong blue component was present in the mean profiles in 2005, but nearly disappeared in 2010. A small residual of this blue component appears to be left in the rms profiles at around $-1500\,\mathrm{km\,s^{-1}}$. The narrow-line subtraction for the campaign of 2010 revealed a red component in the mean profile of Hα at around $\pm 1200\,\mathrm{km\,s^{-1}}$ (see Sect. 3.1) that is also discernible in the Hβ profile (see above). Moreover, the rms profiles show a variable red component with the same velocity. This inner red component is in agreement with a red and slightly stronger component already present in the mean and rms profiles of the campaign in 2004/05. In summary, both the mean and rms profiles of the campaigns in 2004/05 and 2010 show blue and red components at mirrored velocities. These components were stronger in 2004/05. Presumably, these symmetric (with respect to line-of-sight velocity) components are the signature of an accretion disk as accretion disks are expected to result in double-peaked profiles (e.g., Horne & Marsh 1986; Eracleous & Halpern 2003; Gezari et al. 2007; Shapovalova et al. 2013; Storchi-Bergmann et al. 2017, and references therein).

The highly variable outer rms Balmer satellite components were also present in 2005, but are more pronounced in 2010. Such variable outer line-components are very rare and have been seen only in the rms profiles of a few broad-line radio galaxies, for example, 3C390.3, Arp102B, 3C382, or 3C332 (Gezari et al. 2007). Mrk 926 shows a radio flux of $18 \pm 5\,\mathrm{mJy}$ at 5 Ghz (Bicay et al. 1995). The optical B-band flux is 6.6 mJy (McAlary et al. 1983). Therefore, the radio-to-optical luminosity $R(F(5\,\mathrm{Ghz})/F(B\text{-band}))$ has a value of 3. This is above the definition for a radio-quiet AGN (R: $0.1-1$) and below the value for a radio-loud AGN (R: $10-1000$) (Kellermann et al. 1989). However, the highly variable outer components in the rms profiles shown by Gezari et al. (2007) are almost exclusively connected to the flanks of the double-peaked mean profiles, which are assumed to originate from an accretion disk. This is not the case for Mrk 926. Instead, the rms components are further out and their position overlaps with the outer line-wings, but not the line-flanks (see Fig. 8).

4.4. Central black hole mass and Eddington ratio, L/L_{edd}

In Sect. 3.7, we derived a central BH mass of $1.1 \times 10^8\,M_\odot$. This is a normal BH mass in the typical range of $10^6-10^9\,M_\odot$ (e.g., Woo & Urry 2002; Peterson et al. 2004). In the following, we derive the Eddington ratios, L/L_{edd}, for the low and high intensity state of Mrk 926 during our variability campaign. The optical luminosity of Mrk 926 during the low state in November 2010 was by a factor of 2.8 lower with respect to the high state in August 2010. We derive bolometric luminosities of $L_{\mathrm{bol}}(\mathrm{max}) = 1.2 \times 10^{45}\,\mathrm{erg\,s^{-1}}$ and $L_{\mathrm{bol}}(\mathrm{min}) = 4.3 \times 10^{44}\,\mathrm{erg\,s^{-1}}$ for the high and low state, respectively, based on the monochromatic luminosity L_{5100} and on an average bolometric correction factor of $f_{\mathrm{bol}} = L_{\mathrm{bol}}/L_{5100} = 10$ (Kaspi et al. 2000; Castelló-Mor et al. 2016). Although the boundary between Seyfert galaxies and the higher luminosity quasars is not well defined, a bolometric luminosity of $L_{\mathrm{bol}} = 10^{45}\,\mathrm{erg\,s^{-1}}$ of the central source is often used as a dividing line to distinguish between these two types (Netzer 2013). This places Mrk 926 directly at the dividing line, hence being, depending on the time of observation, either a very strong Seyfert 1 galaxy or a quasar.

The BH mass of $1.1 \times 10^8\,M_\odot$ corresponds to an Eddington luminosity of $L_{\mathrm{edd}} = 1.4 \times 10^{46}\,\mathrm{erg\,s^{-1}}$. Therefore, the Eddington ratios, L/L_{edd}, for the high and low state have comparatively low values, 8 and 3 percent only. Such low Eddington ratios of a few percent are typical for highly variable objects. For example, the changing-look AGN IRAS 23226-3843 showed a low Eddington ratio of only one percent (Kollatschny et al. 2020). This low Eddington ratio is consistent with investigations of Noda & Done (2018) and MacLeod et al. (2019). In particular, Noda & Done (2018) suggested that all changing-look AGN are associated with state transitions at Eddington ratios of a few percent.

4.5. Structure and kinematics of the BLR

4.5.1. CCFs of the central, blue, and red line segments

The CCFs of the integrated Balmer line light curves and of the central Balmer line component light curves (within $\pm 5000\,\mathrm{km\,s^{-1}}$) exhibit two discrete peaks, one at a delay of ~ 10 days (Hα) and ~ 5 days (Hβ), and the outer at a delay of ~ 56 days (Hα) and ~ 48 days (Hβ). The long-delay peaks of Hα and Hβ indicate a stratification of the BLR as the CCFs peak at 57^{+3}_{-3} and 48^{+7}_{-6} days, respectively. The blue and red Balmer segment light curves (i.e., the light curves of the Balmer satellite components) are single-peaked, with delays of ~ 4 days for Hα and ~ 5 days for Hβ. This means that the outer wings respond promptly to the variations in the continuum.

The HeI $\lambda 5876$ line shows no double-peaked CCF. Instead, the CCF of the central line profile light curve shows a very broad peak with high correlations up to ~ 40 days. This broad peak might be caused by two merging peaks (i.e., by two independently responding components exactly as observed for Hα and Hβ) but with relatively broad transfer functions that our campaign was not able to resolve.

4.5.2. Velocity-resolved CCFs of the Balmer lines

The velocity-resolved CCFs of Hα and Hβ (Figs. 10a and b) are, in essence, similar to each other. The delays of the central profiles and of the outer wings are all confined within the virial envelope for a Keplerian disk inclined by $\sim 50°$ with a central mass of $1.1 \times 10^8\,M_\odot$. Signatures outside of the virial envelopes can be attributed to relatively strong narrow-line residuals (e.g., in the red wing of Hβ), to overlapping velocity-resolved line signatures (e.g., of He II $\lambda 4686$ and Hβ), or to strong absorption disturbing the segment light curves (e.g., in the outermost blue wing of Hα). Both velocity-resolved CCFs show a broad inner delay region with small time lags of $\sim 3-10$ days. The correlation is strongest in the line wings beyond $\pm 5000\,\mathrm{km\,s^{-1}}$, exactly where we observed the maximum of the additional, varying Balmer satellites in the rms profiles. These Balmer satellites respond promptly to the continuum variations with delays of only $\sim 3-5$ days.

The Hα line shows two velocity-delay structures in the central segment (within $\pm 5000\,\mathrm{km\,s^{-1}}$) at 10^{+3}_{-2} and 57^{+3}_{-3} light-days. This might be interpreted as the upper and lower half of an ellipse in the velocity-delay plane, which might be the signature of a line-emitting ring orbiting the BH at a radius $R = 33.5$ light-days. This interpretation of the two velocity-delay structures being the signature of a line-emitting ring is analogous to that of the velocity-delay maps of NGC 5548 based on the STORM campaign (Horne et al. 2021), and is in turn supported by our finding that the line profiles in Mrk 926 show the signature of

an accretion disk (see Sect. 4.3). Likewise, the Hβ line shows two velocity-delay structures in the central region at 5^{+2}_{-2} and 48^{+7}_{-6} light-days, although less pronounced. The possible line-emitting ring orbiting the BH has a radius of R = 26.5 light-days. However, the relative strength of the responses of the near and far side of the ring is different in Hα and Hβ. This might be caused by optical depths effects. Moreover, Hα shows a strong discontinuity between the signature of the central line profile and the Balmer satellites, which is less pronounced in the velocity-resolved CCF of Hβ. This might be due to interference of Hβ with the He II λ4686 line.

Assuming the two Balmer velocity-delay structures to be the signature of an inclined accretion disk, we determined a mean inclination angle of $i \sim 50°$. This rather high inclination angle is supported by the remarkably broad emission lines ($\sim$30 000 km s^{-1} FWZI) in Mrk 926.

4.5.3. Origin of the Balmer satellites

The existence of the additional, fast-response Balmer satellite components in the rms line profiles and in the velocity-resolved CCFs is an indication for an additional line-emitting component in the nuclear region that might not be directly connected to the accretion disk. Because of the clear separation between the central and outer components, their differing variability behavior, the clearly distinct time lags, as well as the outer rms component not being connected to the line-flanks, we propose that the Balmer satellite components may originate in a region that is spatially distinct from the rest of the BLR. For example, the outer wing components might be connected with a different spatial region like a hollow outflow cone with a high tilt angle or small-scale central radio jets. Notably, Ulvestad & Wilson (1984) found a slightly resolved radio source for Mrk 926 with the VLA at 6 cm. Mundell et al. (2000) suggested additional extended radio emission on scales between about 2 and 260 mas based on observations with the VLBA and VLA and the comparison of their radio beams.

5. Summary

We present results of a spectroscopic and photometric monitoring campaign of the very broad-line AGN Mrk 926, which was carried out with the 10m HET telescope and the Wise Observatory in 2010. Our findings can be summarized as follows:

(1) Mrk 926 is a highly variable AGN. The continuum luminosity showed a drastic decrease during our campaign. It dropped to less than 50% of its original luminosity within only 2.5 months.

(2) Mrk 926 shows very broad Hα and Hβ line profiles, with additional outer Balmer satellite components ranging from ±5000 to ±13 000 km s^{-1} that are clearly discernible in the rms spectra.

(3) The Balmer lines show two velocity-delay structures in their central line component (within ±5000 km s^{-1}), at $\sim$10 and $\sim$57 light-days (Hα) and at $\sim$5 and $\sim$48 light-days (Hβ). These structures might be interpreted as the upper and lower halves of an ellipse in the velocity-delay plane, which might be the signature of a line-emitting ring orbiting the BH at radii, R, of 33.5 and 26.5 light-days.

(4) The continuum luminosities log(λL_λ/erg s^{-1}) at 5180 Å (rest frame) of 43.68–44.13 are in good agreement with the established $R_{BLR} - L_{AGN}$ relation.

(5) The derived BH mass of $1.1\times10^8\ M_\odot$ indicates a low Eddington ratio, which decreased from 8 to 3 percent within only 2.5 months.

(6) Based on the comparison of the variability behavior of the central line component and the outer line wings, we speculate that the outer emission components (the Balmer satellites) originate in a different, spatially distinct region.

Further densely sampled spectroscopic and photometric studies of this highly variable AGN are desirable.

References

Ahumada, R., Prieto, C. A., Almeida, A., et al. 2020, ApJS, 249, 3
Barth, A. J., Pancoast, A., Thorman, S. J., et al. 2011, ApJ, 743, L4
Bentz, M. C., Walsh, J. L., Barth, A. J., et al. 2008, ApJ, 689, L21
Bentz, M. C., Denney, K. D., Grier, C. J., et al. 2013, ApJ, 767, 149
Bessell, M. S. 1990, PASP, 102, 1181
Bicay, M. D., Kojoian, G., Seal, J., Dickinson, D. F., & Malkan, M. A. 1995, ApJS, 98, 369
Brosch, N., Polishook, D., Shporer, A., et al. 2008, Ap&SS, 314, 163
Castelló-Mor, N., Netzer, H., & Kaspi, S. 2016, MNRAS, 458, 1839
Choloniewski, J. 1981, Acta Astron., 31, 293
Denney, K. D., Peterson, B. M., Pogge, R. W., et al. 2009, ApJ, 704, L80
Du, P., Brotherton, M. S., Wang, K., et al. 2018, ApJ, 869, 142
Durret, F., & Bergeron, J. 1988, A&AS, 75, 273
Edelson, R. A., & Krolik, J. H. 1988, ApJ, 333, 646
Edelson, R., Turner, T. J., Pounds, K., et al. 2002, ApJ, 568, 610
Eracleous, M., & Halpern, J. P. 2003, ApJ, 599, 886
Fromerth, M. J., & Melia, F. 2000, ApJ, 533, 172
Garnier, R., Paturel, G., Petit, C., Marthinet, M. C., & Rousseau, J. 1996, A&AS, 117, 467
Gaskell, C. M., & Harrington, P. Z. 2018, MNRAS, 478, 1660
Gezari, S., Halpern, J. P., & Eracleous, M. 2007, ApJS, 169, 167
Graham, A. W., Onken, C. A., Athanassoula, E., & Combes, F. 2011, MNRAS, 412, 2211
Grier, C. J., Peterson, B. M., Pogge, R. W., et al. 2012, ApJ, 755, 60
Grier, C. J., Peterson, B. M., Horne, K., et al. 2013a, ApJ, 764, 47
Grier, C. J., Martini, P., Watson, L. C., et al. 2013b, ApJ, 773, 90
Grier, C. J., Trump, J. R., Shen, Y., et al. 2017, ApJ, 851, 21
Haas, M., Chini, R., Ramolla, M., et al. 2011, A&A, 535, A73
Hao, L., Strauss, M. A., Tremonti, C. A., et al. 2005, AJ, 129, 1783
Horne, K., & Marsh, T. R. 1986, MNRAS, 218, 761
Horne, K., De Rosa, G., Peterson, B. M., et al. 2021, ApJ, 907, 76
Kaspi, S., Smith, P. S., Netzer, H., et al. 2000, ApJ, 533, 631
Kaspi, S., Maoz, D., Netzer, H., et al. 2005, ApJ, 629, 61
Kellermann, K. I., Sramek, R., Schmidt, M., Shaffer, D. B., & Green, R. 1989, AJ, 98, 1195
Kilerci Eser, E., Vestergaard, M., Peterson, B. M., Denney, K. D., & Bentz, M. C. 2015, ApJ, 801, 8
Kollatschny, W. 2003, A&A, 407, 461
Kollatschny, W., & Bischoff, K. 2002, A&A, 386, L19
Kollatschny, W., & Dietrich, M. 1997, A&A, 323, 5
Kollatschny, W., & Fricke, K. J. 1985, A&A, 146, L11
Kollatschny, W., & Zetzl, M. 2010, A&A, 522, A36
Kollatschny, W., & Zetzl, M. 2011, Nature, 470, 366
Kollatschny, W., & Zetzl, M. 2013, A&A, 549, A100
Kollatschny, W., Fricke, K. J., Schleicher, H., & Yorke, H. W. 1981, A&A, 102, L23
Kollatschny, W., Bischoff, K., & Dietrich, M. 2000, A&A, 361, 901
Kollatschny, W., Bischoff, K., Robinson, E. L., Welsh, W. F., & Hill, G. J. 2001, A&A, 379, 125
Kollatschny, W., Zetzl, M., & Dietrich, M. 2006, A&A, 454, 459
Kollatschny, W., Ulrich, K., Zetzl, M., Kaspi, S., & Haas, M. 2014, A&A, 566, A106
Kollatschny, W., Ochmann, M. W., Zetzl, M., et al. 2018, A&A, 619, A168
Kollatschny, W., Grupe, D., Parker, M. L., et al. 2020, A&A, 638, A91

Koratkar, A. P., & Gaskell, C. M. 1991, ApJ, 370, L61
Korista, K. T., & Goad, M. R. 2004, ApJ, 606, 749
MacLeod, C. L., Green, P. J., Anderson, S. F., et al. 2019, ApJ, 874, 8
McAlary, C. W., McLaren, R. A., McGonegal, R. J., & Maza, J. 1983, ApJS, 52, 341
Morris, S. L., & Ward, M. J. 1988, MNRAS, 230, 639
Mundell, C. G., Wilson, A. S., Ulvestad, J. S., & Roy, A. L. 2000, ApJ, 529, 816
Netzer, H. 2013, The Physics and Evolution of Active Galactic Nuclei
Netzer, H., Heller, A., Loinger, F., et al. 1996, MNRAS, 279, 429
Noda, H., & Done, C. 2018, MNRAS, 480, 3898
Onken, C. A., Ferrarese, L., Merritt, D., et al. 2004, ApJ, 615, 645
Osterbrock, D. E., & Shuder, J. M. 1982, ApJS, 49, 149
Peterson, B. M., Wanders, I., Bertram, R., et al. 1998, ApJ, 501, 82
Peterson, B. M., Berlind, P., Bertram, R., et al. 2002, ApJ, 581, 197
Peterson, B. M., Ferrarese, L., Gilbert, K. M., et al. 2004, ApJ, 613, 682
Rehfeld, K., Marwan, N., Heitzig, J., & Kurths, J. 2011, Nonlinear Processes Geophys., 18, 389
Rodríguez-Pascual, P. M., Alloin, D., Clavel, J., et al. 1997, ApJS, 110, 9
Sakata, Y., Minezaki, T., Yoshii, Y., et al. 2010, ApJ, 711, 461
Schlafly, E. F., & Finkbeiner, D. P. 2011, ApJ, 737, 103
Sergeev, S. G., Pronik, V. I., Peterson, B. M., Sergeeva, E. A., & Zheng, W. 2002, ApJ, 576, 660
Shakura, N. I., & Sunyaev, R. A. 1973, A&A, 500, 33
Shapovalova, A. I., Popović, L. Č., Burenkov, A. N., et al. 2013, A&A, 559, A10
Shen, Y., Horne, K., Grier, C. J., et al. 2016, ApJ, 818, 30
Stetson, P. B. 1987, PASP, 99, 191
Storchi-Bergmann, T., Schimoia, J. S., Peterson, B. M., et al. 2017, ApJ, 835, 236
Tody, D. 1986, in Instrumentation in Astronomy VI, ed. D. L. Crawford, SPIE Conf. Ser., 627, 733
Tody, D. 1993, in Astronomical Data Analysis Software and Systems II, eds. R. J. Hanisch, R. J. V. Brissenden, & J. Barnes, ASP Conf. Ser., 52, 173
Ulvestad, J. S., & Wilson, A. S. 1984, ApJ, 278, 544
Ward, M. J., Wilson, A. S., Penston, M. V., et al. 1978, ApJ, 223, 788
Winkler, H., Glass, I. S., van Wyk, F., et al. 1992, MNRAS, 257, 659
Woo, J.-H., & Urry, C. M. 2002, ApJ, 579, 530
Wright, E. L. 2006, PASP, 118, 1711
Xiao, M., Du, P., Horne, K., et al. 2018, ApJ, 864, 109
Zetzl, M., Kollatschny, W., Ochmann, M. W., et al. 2018, A&A, 618, A83

Appendix A: Additional figures

Fig. A.1. Light curves of the combined continuum flux densities at 5420 Å (observed frame; in units of 10^{-15} erg cm^{-2} s^{-1} Å^{-1}) as well as of the Hα segment (center, blue, red) light curves.

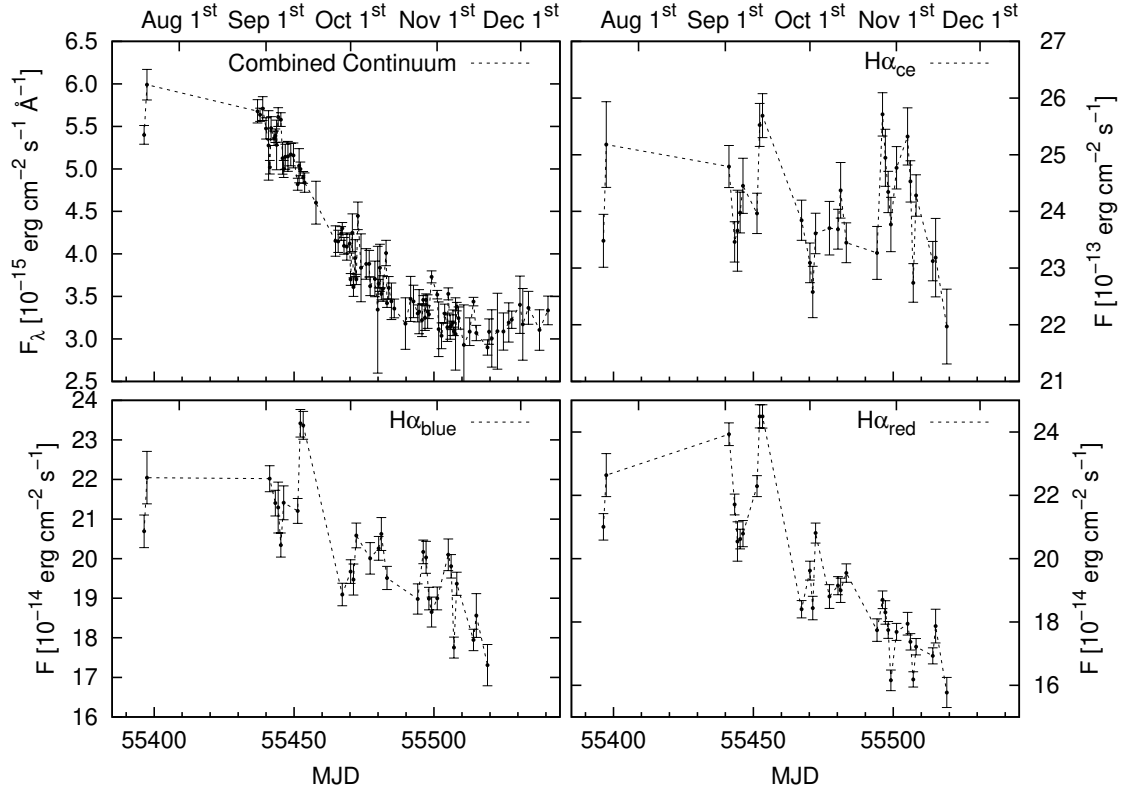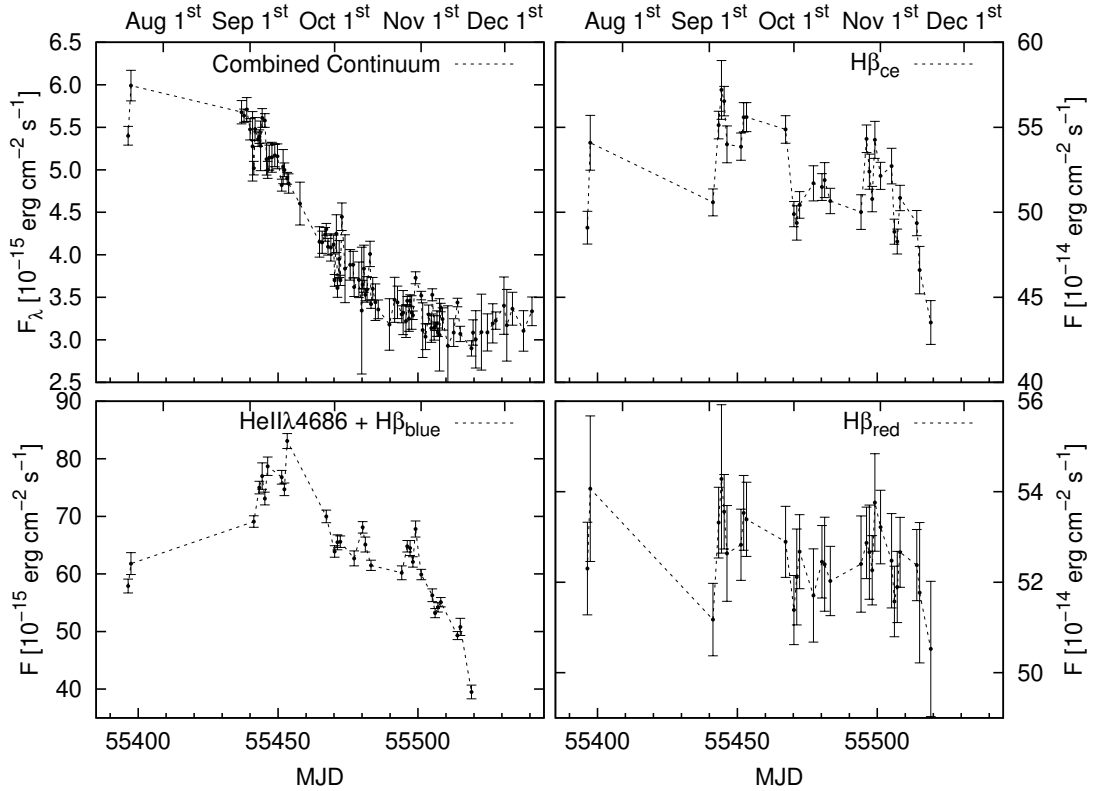**Fig. A.2.** Light curves of the combined continuum flux densities at 5420 Å (observed frame; in units of 10^{-15} erg cm^{-2} s^{-1} Å^{-1}) as well as of the Hβ segment (center, blue, red) light curves.

Appendix B: Additional tables

Table B.1. HET continuum flux densities (observed frame).

Mod. Julian Date (1)	Cont. 4425 Å (2)	Cont. 4755 Å (3)	Cont. 5420 Å (4)	Cont. 5485 Å (5)	Cont. 5755 Å (6)	Cont. 6530 Å (7)	Cont. 7255 Å (8)
55396.41	8.12 ± 0.16	7.07 ± 0.14	5.40 ± 0.11	5.39 ± 0.11	4.95 ± 0.10	4.65 ± 0.09	4.22 ± 0.08
55397.42	8.73 ± 0.26	7.73 ± 0.23	5.99 ± 0.18	5.94 ± 0.18	5.44 ± 0.16	4.92 ± 0.15	4.48 ± 0.13
55441.31	7.49 ± 0.11	6.61 ± 0.10	5.02 ± 0.08	4.99 ± 0.07	4.60 ± 0.07	4.30 ± 0.06	4.27 ± 0.06
55443.30	7.44 ± 0.11	6.85 ± 0.10	5.39 ± 0.08	5.41 ± 0.08	4.96 ± 0.07	4.53 ± 0.07	4.29 ± 0.06
55444.30	7.73 ± 0.15	7.04 ± 0.14	5.61 ± 0.11	5.66 ± 0.11	5.28 ± 0.11	4.43 ± 0.09	4.40 ± 0.09
55445.28	7.76 ± 0.12	6.99 ± 0.10	5.58 ± 0.08	5.62 ± 0.08	5.27 ± 0.08	4.29 ± 0.06	4.63 ± 0.07
55446.29	7.43 ± 0.15	6.59 ± 0.13	5.00 ± 0.10	5.00 ± 0.10	4.57 ± 0.09	4.30 ± 0.09	4.31 ± 0.09
55451.27	7.09 ± 0.11	6.26 ± 0.09	4.82 ± 0.07	4.84 ± 0.07	4.43 ± 0.07	4.03 ± 0.06	4.03 ± 0.06
55452.26	6.25 ± 0.09	5.95 ± 0.09	5.00 ± 0.08	5.03 ± 0.08	4.77 ± 0.07	4.19 ± 0.06	3.91 ± 0.06
55453.26	7.04 ± 0.11	6.19 ± 0.09	4.90 ± 0.07	4.90 ± 0.07	4.57 ± 0.07	4.07 ± 0.06	4.01 ± 0.06
55467.23	5.41 ± 0.08	5.03 ± 0.08	4.30 ± 0.07	4.37 ± 0.07	4.09 ± 0.06	3.51 ± 0.05	4.03 ± 0.06
55470.21	5.32 ± 0.08	4.69 ± 0.07	3.70 ± 0.07	3.73 ± 0.06	3.47 ± 0.05	3.31 ± 0.05	3.47 ± 0.05
55471.21	4.98 ± 0.15	4.48 ± 0.13	3.61 ± 0.11	3.65 ± 0.11	3.40 ± 0.10	3.33 ± 0.10	3.31 ± 0.10
55472.22	4.57 ± 0.07	4.34 ± 0.07	3.70 ± 0.06	3.77 ± 0.06	3.54 ± 0.05	3.31 ± 0.05	3.34 ± 0.05
55477.20	4.83 ± 0.14	4.46 ± 0.13	3.62 ± 0.11	3.67 ± 0.11	3.40 ± 0.10	3.36 ± 0.10	3.45 ± 0.10
55480.20	4.40 ± 0.07	4.23 ± 0.06	3.65 ± 0.05	3.74 ± 0.06	3.53 ± 0.05	3.44 ± 0.05	3.45 ± 0.05
55481.20	4.59 ± 0.09	4.21 ± 0.08	3.53 ± 0.07	3.56 ± 0.07	3.32 ± 0.07	3.26 ± 0.07	3.32 ± 0.07
55483.20	4.76 ± 0.07	4.23 ± 0.06	3.42 ± 0.05	3.45 ± 0.05	3.24 ± 0.05	3.04 ± 0.05	3.31 ± 0.05
55494.16	4.12 ± 0.12	3.78 ± 0.11	3.30 ± 0.10	3.35 ± 0.10	3.15 ± 0.09	3.10 ± 0.09	3.18 ± 0.10
55496.15	4.23 ± 0.06	3.98 ± 0.06	3.46 ± 0.05	3.51 ± 0.05	3.26 ± 0.05	3.13 ± 0.05	3.39 ± 0.05
55497.16	4.25 ± 0.09	3.95 ± 0.08	3.46 ± 0.07	3.50 ± 0.07	3.29 ± 0.07	3.26 ± 0.06	3.31 ± 0.07
55498.17	4.28 ± 0.06	3.88 ± 0.06	3.29 ± 0.05	3.35 ± 0.05	3.16 ± 0.05	3.03 ± 0.05	3.31 ± 0.05
55499.16	4.36 ± 0.09	4.18 ± 0.08	3.73 ± 0.07	3.84 ± 0.08	3.62 ± 0.07	3.42 ± 0.07	3.48 ± 0.07
55501.14	4.07 ± 0.06	3.89 ± 0.06	3.52 ± 0.05	3.60 ± 0.05	3.45 ± 0.05	3.02 ± 0.05	3.46 ± 0.05
55505.12	4.26 ± 0.09	4.03 ± 0.08	3.53 ± 0.07	3.57 ± 0.07	3.41 ± 0.07	3.12 ± 0.06	3.34 ± 0.07
55506.12	4.05 ± 0.06	3.72 ± 0.06	3.16 ± 0.05	3.18 ± 0.05	2.96 ± 0.04	3.07 ± 0.05	3.10 ± 0.05
55507.11	4.27 ± 0.06	3.81 ± 0.06	3.09 ± 0.05	3.14 ± 0.05	2.92 ± 0.04	2.86 ± 0.04	3.04 ± 0.05
55508.11	4.13 ± 0.06	3.92 ± 0.06	3.38 ± 0.05	3.46 ± 0.05	3.25 ± 0.05	3.13 ± 0.05	3.31 ± 0.05
55514.12	4.26 ± 0.06	3.93 ± 0.06	3.44 ± 0.05	3.52 ± 0.05	3.34 ± 0.05	2.86 ± 0.04	3.32 ± 0.05
55515.12	4.01 ± 0.12	3.57 ± 0.11	3.07 ± 0.09	3.12 ± 0.09	2.91 ± 0.09	2.89 ± 0.09	2.95 ± 0.09
55519.10	3.93 ± 0.12	3.52 ± 0.11	2.90 ± 0.09	2.96 ± 0.09	2.72 ± 0.08	2.76 ± 0.08	2.96 ± 0.09

Notes. Continuum flux densities in units of 10^{-15} erg s^{-1} cm^{-2} Å^{-1}.

Table B.2. Integrated broad-line fluxes – including the narrow components – of the Balmer and helium lines for different epochs.

Mod. Julian Date (1)	Hα (2)	Hβ (3)	Hγ (4)	He I$_{center}$ (5)	He II + Hβ$_{blue}$ (6)
55396.41	2765. ± 55.	1072. ± 21.	152.7 ± 3.1	85.4 ± 2.2	57.9 ± 1.2
55397.42	2965. ± 89.	1143. ± 34.	163.6 ± 4.9	93.0 ± 1.4	61.8 ± 1.9
55441.31	2939. ± 44.	1087. ± 17.	136.6 ± 2.1	96.6 ± 1.5	69.1 ± 1.0
55443.30	2777. ± 42.	1160. ± 17.	129.6 ± 1.9	105.0 ± 2.7	75.0 ± 1.1
55444.30	2784. ± 84.	1192. ± 36.	129.7 ± 3.9	115.8 ± 1.8	77.0 ± 2.3
55445.28	2808. ± 42.	1174. ± 18.	147.3 ± 2.2	109.1 ± 2.8	73.1 ± 1.1
55446.29	2867. ± 57.	1145. ± 23.	146.6 ± 2.9	93.7 ± 1.5	78.7 ± 1.6
55451.27	2832. ± 42.	1144. ± 17.	157.6 ± 2.4	98.8 ± 2.0	76.8 ± 1.2
55452.26	3032. ± 45.	1166. ± 18.	138.2 ± 2.1	132.2 ± 2.0	74.7 ± 1.1
55453.26	3048. ± 46.	1173. ± 18.	160.6 ± 2.4	121.5 ± 1.9	83.1 ± 1.3
55467.23	2759. ± 41.	1148. ± 17.	155.5 ± 2.3	104.6 ± 1.6	70.0 ± 1.1
55470.21	2702. ± 41.	1077. ± 16.	152.4 ± 2.3	92.4 ± 1.4	63.9 ± 1.0
55471.21	2637. ± 53.	1080. ± 22.	156.6 ± 3.1	99.4 ± 1.5	65.5 ± 1.3
55472.22	2775. ± 42.	1097. ± 17.	155.0 ± 2.3	106.2 ± 1.6	65.6 ± 1.0
55477.20	2759. ± 55.	1104. ± 22.	163.5 ± 3.3	98.8 ± 2.0	62.7 ± 1.3
55480.20	2763. ± 41.	1115. ± 17.	164.4 ± 2.5	105.5 ± 1.6	68.1 ± 1.0
55481.20	2834. ± 57.	1108. ± 22.	173.4 ± 3.5	101.3 ± 1.6	65.1 ± 1.3
55483.20	2735. ± 41.	1088. ± 16.	178.4 ± 2.7	93.7 ± 1.5	61.5 ± 0.9
55494.16	2694. ± 54.	1084. ± 22.	164.6 ± 3.3	89.8 ± 1.8	60.2 ± 1.2
55496.15	2960. ± 44.	1137. ± 17.	183.5 ± 2.8	92.2 ± 1.4	64.8 ± 1.0
55497.16	2878. ± 58.	1115. ± 22.	184.7 ± 3.7	92.7 ± 1.9	64.5 ± 1.3
55498.17	2802. ± 42.	1093. ± 16.	187.8 ± 2.8	85.0 ± 1.7	62.1 ± 0.9
55499.16	2725. ± 55.	1148. ± 23.	192.1 ± 3.8	93.1 ± 2.4	67.8 ± 1.4
55501.14	2844. ± 43.	1114. ± 17.	181.2 ± 2.7	92.3 ± 1.4	59.9 ± 0.9
55505.12	2913. ± 58.	1108. ± 22.	190.3 ± 3.8	94.7 ± 2.4	56.3 ± 1.1
55506.12	2825. ± 42.	1058. ± 16.	166.1 ± 2.5	85.1 ± 1.3	53.2 ± 0.8
55507.11	2613. ± 39.	1056. ± 16.	180.3 ± 2.7	73.1 ± 1.1	54.2 ± 0.8
55508.11	2794. ± 42.	1090. ± 16.	177.6 ± 2.7	86.3 ± 1.3	55.1 ± 0.8
55514.12	2661. ± 40.	1067. ± 16.	159.9 ± 2.4	85.8 ± 1.3	49.3 ± 0.7
55515.12	2683. ± 80.	1035. ± 31.	148.3 ± 4.4	79.7 ± 1.2	50.8 ± 1.5
55519.10	2528. ± 76.	980. ± 29.	143.8 ± 4.3	66.8 ± 1.0	39.5 ± 1.2

Notes. Line fluxes in units of 10^{-15} erg s^{-1} cm^{-2}.

Table B.3. HET continuum light curves used for the FVG method (observed frame).

Mod. Julian Date	Cont. 4425 Å [mJy]	Cont. 4425 Å ext. corr.	Cont. 4425 Å [mJy]	Cont. 4425 Å ext. corr.	Cont. 5420 Å	Cont. 5420 Å ext. corr.	Cont. 5420 Å [mJy]	Cont. 5420 Å ext. corr.	Cont. 6530 Å	Cont. 6530 Å ext. corr.	Cont. 6530 Å [mJy]	Cont. 6530 Å ext. corr.
(1)	(2)	(3)	(4)	(5)	(6)	(7)	(8)	(9)	(10)	(11)	(12)	(13)
55396.41	8.12 ± 0.16	9.31 ± 0.19	5.30 ± 0.11	6.08 ± 0.12	5.40 ± 0.11	5.99 ± 0.13	5.29 ± 0.11	5.87 ± 0.12	4.65 ± 0.09	5.05 ± 0.10	6.61 ± 0.13	7.18 ± 0.14
55397.42	8.73 ± 0.26	10.01 ± 0.30	5.70 ± 0.17	6.54 ± 0.20	5.99 ± 0.18	6.65 ± 0.20	5.87 ± 0.18	6.51 ± 0.20	4.92 ± 0.15	5.34 ± 0.17	7.00 ± 0.22	7.60 ± 0.24
55441.31	7.49 ± 0.11	8.59 ± 0.13	4.89 ± 0.08	5.61 ± 0.09	5.02 ± 0.08	5.57 ± 0.09	4.92 ± 0.08	5.46 ± 0.09	4.30 ± 0.06	4.67 ± 0.07	6.12 ± 0.09	6.64 ± 0.10
55443.30	7.44 ± 0.11	8.53 ± 0.13	4.86 ± 0.08	5.57 ± 0.09	5.39 ± 0.08	5.98 ± 0.09	5.28 ± 0.08	5.86 ± 0.09	4.53 ± 0.07	4.92 ± 0.08	6.44 ± 0.10	6.99 ± 0.11
55444.30	7.73 ± 0.15	8.87 ± 0.18	5.05 ± 0.10	5.79 ± 0.12	5.61 ± 0.11	6.23 ± 0.13	5.50 ± 0.11	6.10 ± 0.12	4.43 ± 0.09	4.81 ± 0.10	6.30 ± 0.13	6.84 ± 0.14
55445.28	7.76 ± 0.12	8.90 ± 0.14	5.07 ± 0.08	5.81 ± 0.09	5.58 ± 0.08	6.19 ± 0.09	5.47 ± 0.08	6.07 ± 0.09	4.29 ± 0.06	4.66 ± 0.07	6.10 ± 0.09	6.62 ± 0.10
55446.29	7.43 ± 0.15	8.52 ± 0.18	4.85 ± 0.10	5.57 ± 0.12	5.00 ± 0.10	5.55 ± 0.12	4.90 ± 0.10	5.44 ± 0.11	4.30 ± 0.09	4.67 ± 0.10	6.12 ± 0.13	6.64 ± 0.14
55451.27	7.09 ± 0.11	8.13 ± 0.13	4.63 ± 0.08	5.31 ± 0.09	4.82 ± 0.07	5.35 ± 0.08	4.72 ± 0.07	5.24 ± 0.08	4.03 ± 0.06	4.37 ± 0.07	5.73 ± 0.09	6.22 ± 0.10
55452.26	6.25 ± 0.09	7.17 ± 0.11	4.08 ± 0.06	4.68 ± 0.07	5.00 ± 0.08	5.55 ± 0.09	4.90 ± 0.08	5.44 ± 0.09	4.19 ± 0.06	4.55 ± 0.07	5.96 ± 0.09	6.47 ± 0.10
55453.26	7.04 ± 0.11	8.08 ± 0.13	4.60 ± 0.08	5.27 ± 0.09	4.90 ± 0.07	5.44 ± 0.08	4.80 ± 0.07	5.33 ± 0.08	4.07 ± 0.06	4.42 ± 0.07	5.79 ± 0.09	6.28 ± 0.10
55467.23	5.41 ± 0.08	6.21 ± 0.10	3.53 ± 0.06	4.05 ± 0.06	4.30 ± 0.07	4.77 ± 0.08	4.21 ± 0.07	4.68 ± 0.08	3.51 ± 0.05	3.81 ± 0.06	4.99 ± 0.08	5.42 ± 0.08
55470.21	5.32 ± 0.08	6.10 ± 0.10	3.47 ± 0.06	3.99 ± 0.06	3.70 ± 0.07	4.11 ± 0.08	3.63 ± 0.07	4.02 ± 0.08	3.31 ± 0.05	3.59 ± 0.06	4.71 ± 0.08	5.11 ± 0.08
55471.21	4.98 ± 0.15	5.71 ± 0.18	3.25 ± 0.10	3.73 ± 0.12	3.61 ± 0.11	4.01 ± 0.13	3.54 ± 0.11	3.93 ± 0.12	3.33 ± 0.10	3.61 ± 0.11	4.74 ± 0.15	5.14 ± 0.16
55472.22	4.57 ± 0.07	5.24 ± 0.09	2.98 ± 0.05	3.42 ± 0.06	3.70 ± 0.06	4.11 ± 0.07	3.63 ± 0.06	4.02 ± 0.07	3.31 ± 0.05	3.59 ± 0.06	4.71 ± 0.08	5.11 ± 0.08
55477.20	4.83 ± 0.14	5.54 ± 0.17	3.15 ± 0.10	3.62 ± 0.11	3.62 ± 0.11	4.02 ± 0.13	3.55 ± 0.11	3.94 ± 0.12	3.36 ± 0.10	3.65 ± 0.11	4.78 ± 0.15	5.19 ± 0.16
55480.20	4.40 ± 0.07	5.05 ± 0.09	2.87 ± 0.05	3.30 ± 0.06	3.65 ± 0.05	4.05 ± 0.06	3.58 ± 0.05	3.97 ± 0.06	3.44 ± 0.05	3.73 ± 0.06	4.89 ± 0.08	5.31 ± 0.08
55481.20	4.59 ± 0.09	5.27 ± 0.11	3.00 ± 0.06	3.44 ± 0.07	3.53 ± 0.07	3.92 ± 0.08	3.46 ± 0.08	3.84 ± 0.08	3.26 ± 0.07	3.54 ± 0.08	4.64 ± 0.10	5.03 ± 0.11
55483.20	4.76 ± 0.07	5.46 ± 0.09	3.11 ± 0.05	3.57 ± 0.06	3.42 ± 0.05	3.80 ± 0.06	3.35 ± 0.05	3.72 ± 0.06	3.04 ± 0.05	3.30 ± 0.06	4.32 ± 0.08	4.69 ± 0.08
55494.16	4.12 ± 0.12	4.73 ± 0.14	2.69 ± 0.08	3.09 ± 0.09	3.30 ± 0.10	3.66 ± 0.12	3.23 ± 0.10	3.59 ± 0.11	3.10 ± 0.09	3.36 ± 0.10	4.41 ± 0.13	4.79 ± 0.14
55496.15	4.23 ± 0.06	4.85 ± 0.07	2.76 ± 0.04	3.17 ± 0.05	3.46 ± 0.05	3.84 ± 0.06	3.39 ± 0.05	3.76 ± 0.06	3.13 ± 0.05	3.40 ± 0.06	4.45 ± 0.08	4.83 ± 0.08
55497.16	4.25 ± 0.09	4.88 ± 0.11	2.78 ± 0.06	3.18 ± 0.07	3.46 ± 0.07	3.84 ± 0.08	3.39 ± 0.07	3.76 ± 0.08	3.26 ± 0.06	3.54 ± 0.07	4.64 ± 0.09	5.03 ± 0.10
55498.17	4.28 ± 0.06	4.91 ± 0.07	2.80 ± 0.04	3.21 ± 0.05	3.29 ± 0.05	3.65 ± 0.06	3.22 ± 0.05	3.58 ± 0.06	3.03 ± 0.05	3.29 ± 0.06	4.31 ± 0.08	4.68 ± 0.08
55499.16	4.36 ± 0.09	5.00 ± 0.11	2.85 ± 0.06	3.27 ± 0.07	3.73 ± 0.07	4.14 ± 0.08	3.65 ± 0.07	4.06 ± 0.08	3.42 ± 0.07	3.71 ± 0.08	4.86 ± 0.10	5.28 ± 0.11
55501.14	4.07 ± 0.06	4.67 ± 0.07	2.66 ± 0.04	3.05 ± 0.05	3.52 ± 0.05	3.91 ± 0.06	3.45 ± 0.05	3.83 ± 0.06	3.02 ± 0.05	3.28 ± 0.06	4.30 ± 0.08	4.66 ± 0.08
55505.12	4.26 ± 0.09	4.89 ± 0.11	2.78 ± 0.06	3.19 ± 0.07	3.53 ± 0.07	3.92 ± 0.08	3.46 ± 0.07	3.84 ± 0.08	3.12 ± 0.06	3.39 ± 0.07	4.44 ± 0.09	4.82 ± 0.10
55506.12	4.05 ± 0.06	4.65 ± 0.07	2.65 ± 0.04	3.03 ± 0.05	3.16 ± 0.05	3.51 ± 0.06	3.10 ± 0.05	3.44 ± 0.06	3.07 ± 0.05	3.33 ± 0.06	4.37 ± 0.08	4.74 ± 0.08
55507.11	4.27 ± 0.06	4.90 ± 0.07	2.79 ± 0.04	3.20 ± 0.05	3.09 ± 0.05	3.43 ± 0.06	3.03 ± 0.05	3.36 ± 0.06	2.86 ± 0.04	3.10 ± 0.05	4.07 ± 0.06	4.42 ± 0.07
55508.11	4.13 ± 0.06	4.74 ± 0.07	2.70 ± 0.04	3.09 ± 0.05	3.38 ± 0.05	3.75 ± 0.06	3.31 ± 0.05	3.68 ± 0.06	3.13 ± 0.05	3.40 ± 0.06	4.45 ± 0.08	4.83 ± 0.08
55514.12	4.26 ± 0.06	4.89 ± 0.07	2.78 ± 0.04	3.19 ± 0.05	3.44 ± 0.05	3.82 ± 0.06	3.37 ± 0.05	3.74 ± 0.06	2.86 ± 0.04	3.10 ± 0.05	4.07 ± 0.06	4.42 ± 0.07
55515.12	4.01 ± 0.12	4.60 ± 0.14	2.62 ± 0.08	3.00 ± 0.09	3.07 ± 0.09	3.41 ± 0.10	3.01 ± 0.09	3.34 ± 0.10	2.89 ± 0.09	3.14 ± 0.10	4.11 ± 0.13	4.46 ± 0.14
55519.10	3.93 ± 0.12	4.51 ± 0.14	2.57 ± 0.08	2.94 ± 0.09	2.90 ± 0.09	3.22 ± 0.10	2.84 ± 0.09	3.15 ± 0.10	2.76 ± 0.08	3.00 ± 0.09	3.93 ± 0.12	4.26 ± 0.13

Notes. Unless stated otherwise, the flux is given in 10^{-15} erg s^{-1} cm^{-2} Å^{-1}. In order to calculate the light curves corrected for Galactic extinction, we adopted Galactic extinction values of $A_B = 0.149$, $A_V = 0.113$, and $A_R = 0.089$ from Schlafly & Finkbeiner (2011) (NED).

Table B.4. Combined HET 5420 Å (5180 Å in rest frame) and Wise Observatory V-band light curve.

Mod. Julian Date (1)	Comb. V band [10^{-15} erg s^{-1} cm^{-2} Å^{-1}] (2)	Telescope (3)	Mod. Julian Date (1)	Comb. V band [10^{-15} erg s^{-1} cm^{-2} Å^{-1}] (2)	Telescope (3)
55396.41	5.40 ± 0.11	HET	55481.80	3.59 ± 0.15	Wise
55397.42	5.99 ± 0.18	HET	55482.85	4.01 ± 0.15	Wise
55436.92	5.68 ± 0.14	Wise	55483.20	3.42 ± 0.05	HET
55437.86	5.64 ± 0.08	Wise	55483.82	3.60 ± 0.13	Wise
55438.80	5.71 ± 0.14	Wise	55484.80	3.44 ± 0.21	Wise
55439.96	5.48 ± 0.13	Wise	55485.81	3.36 ± 0.11	Wise
55440.90	5.28 ± 0.41	Wise	55489.79	3.18 ± 0.30	Wise
55441.31	5.02 ± 0.08	HET	55491.66	3.47 ± 0.26	Wise
55441.80	5.48 ± 0.14	Wise	55492.67	3.44 ± 0.19	Wise
55442.88	5.36 ± 0.09	Wise	55494.16	3.30 ± 0.10	HET
55443.30	5.39 ± 0.08	HET	55494.67	3.32 ± 0.26	Wise
55443.78	5.28 ± 0.29	Wise	55495.68	3.22 ± 0.19	Wise
55444.30	5.61 ± 0.11	HET	55496.15	3.46 ± 0.05	HET
55445.28	5.58 ± 0.08	HET	55496.75	3.25 ± 0.15	Wise
55445.92	5.13 ± 0.19	Wise	55497.16	3.46 ± 0.07	HET
55446.29	5.00 ± 0.10	HET	55497.73	3.32 ± 0.20	Wise
55446.84	5.14 ± 0.15	Wise	55498.17	3.29 ± 0.05	HET
55447.81	5.15 ± 0.18	Wise	55499.16	3.73 ± 0.07	HET
55448.81	5.17 ± 0.13	Wise	55501.14	3.52 ± 0.05	HET
55449.78	5.16 ± 0.15	Wise	55501.69	3.11 ± 0.32	Wise
55451.27	4.82 ± 0.07	HET	55502.71	3.04 ± 0.15	Wise
55451.79	5.04 ± 0.20	Wise	55503.79	3.30 ± 0.11	Wise
55452.26	5.00 ± 0.08	HET	55504.79	3.14 ± 0.17	Wise
55453.26	4.90 ± 0.07	HET	55505.12	3.53 ± 0.07	HET
55453.78	4.84 ± 0.11	Wise	55505.76	3.14 ± 0.14	Wise
55457.80	4.60 ± 0.25	Wise	55506.12	3.16 ± 0.05	HET
55464.79	4.15 ± 0.18	Wise	55506.80	3.19 ± 0.15	Wise
55465.76	4.15 ± 0.13	Wise	55507.11	3.09 ± 0.05	HET
55466.85	4.24 ± 0.08	Wise	55507.72	3.06 ± 0.43	Wise
55467.23	4.30 ± 0.07	HET	55508.11	3.38 ± 0.05	HET
55467.84	4.09 ± 0.10	Wise	55508.77	3.25 ± 0.13	Wise
55468.83	4.09 ± 0.16	Wise	55510.66	2.93 ± 0.47	Wise
55469.84	4.12 ± 0.11	Wise	55512.75	3.09 ± 0.16	Wise
55470.21	3.70 ± 0.07	HET	55514.12	3.44 ± 0.05	HET
55470.81	4.25 ± 0.22	Wise	55515.12	3.07 ± 0.09	HET
55471.21	3.61 ± 0.11	HET	55519.10	2.90 ± 0.09	HET
55471.84	3.95 ± 0.22	Wise	55519.69	3.09 ± 0.15	Wise
55472.22	3.70 ± 0.06	HET	55520.65	3.01 ± 0.34	Wise
55472.80	4.45 ± 0.16	Wise	55522.67	3.09 ± 0.45	Wise
55473.92	3.84 ± 0.40	Wise	55524.79	3.09 ± 0.22	Wise
55475.76	3.88 ± 0.18	Wise	55526.71	3.19 ± 0.23	Wise
55476.85	3.88 ± 0.16	Wise	55527.76	3.23 ± 0.10	Wise
55477.20	3.62 ± 0.11	HET	55530.71	3.40 ± 0.34	Wise
55478.89	3.71 ± 0.21	Wise	55531.70	3.17 ± 0.42	Wise
55479.88	3.34 ± 0.75	Wise	55533.75	3.37 ± 0.19	Wise
55480.20	3.65 ± 0.05	HET	55537.67	3.11 ± 0.24	Wise
55480.69	3.84 ± 0.28	Wise	55540.72	3.34 ± 0.17	Wise
55481.20	3.53 ± 0.07	HET			